Initial results from a dynamic coupled magnetosphere-ionosphere-ring current model

Asher Pembroke,[1] Frank Toffoletto,[1] Stanislav Sazykin,[1] Michael Wiltberger,[2] John Lyon,[3] Viacheslav Merkin,[4] and Peter Schmitt[2]

Received 5 July 2011; revised 5 November 2011; accepted 11 December 2011; published 22 February 2012.

[1] In this paper we describe a coupled model of Earth's magnetosphere that consists of the Lyon-Fedder-Mobarry (LFM) global magnetohydrodynamics (MHD) simulation, the MIX ionosphere solver and the Rice Convection Model (RCM) and report some results using idealized inputs and model parameters. The algorithmic and physical components of the model are described, including the transfer of magnetic field information and plasma boundary conditions to the RCM and the return of ring current plasma properties to the LFM. Crucial aspects of the coupling include the restriction of RCM to regions where field-line averaged plasma-$\beta \leq 1$, the use of a plasmasphere model, and the MIX ionosphere model. Compared to stand-alone MHD, the coupled model produces a substantial increase in ring current pressure and reduction of the magnetic field near the Earth. In the ionosphere, stronger region-1 and region-2 Birkeland currents are seen in the coupled model but with no significant change in the cross polar cap potential drop, while the region-2 currents shielded the low-latitude convection potential. In addition, oscillations in the magnetic field are produced at geosynchronous orbit with the coupled code. The diagnostics of entropy and mass content indicate that these oscillations are associated with low-entropy flow channels moving in from the tail and may be related to bursty bulk flows and bubbles seen in observations. As with most complex numerical models, there is the ongoing challenge of untangling numerical artifacts and physics, and we find that while there is still much room for improvement, the results presented here are encouraging.

Citation: Pembroke, A., F. Toffoletto, S. Sazykin, M. Wiltberger, J. Lyon, V. Merkin, and P. Schmitt (2012), Initial results from a dynamic coupled magnetosphere-ionosphere-ring current model, *J. Geophys. Res.*, *117*, A02211, doi:10.1029/2011JA016979.

1. Introduction

1.1. Modeling the Magnetosphere

[2] The need for robust and accurate models of the near-Earth space environment has been met in part through simulating the physics of space plasmas from first principles. Several formulations exist that are tailored for different domains and plasma properties within the magnetosphere, depending on which physics are most relevant. Much of the global morphology has been captured by magnetohydrodynamics (MHD) simulations: when driven by a solar wind specification, MHD simulations are capable of producing shocks, reconnection, as well as storm-time tail and plasma sheet configurations. These models include ionospheric solvers driven by Birkeland currents to determine the convection pattern over the poles. However, close to the Earth, gradient-curvature drift dynamics play an important role in the spatial and energy distributions of the plasma. In this region, ring current models give the most accurate descriptions of the plasma properties. In order to capture both inner and outer magnetospheric physics, a coupling of ring current and MHD simulations has been undertaken. We previously reported on the one-way coupling of the Lyon Fedder Mobarry (LFM) magnetohydrodynamics (MHD) simulation of the Earth's magnetosphere with the Rice Convection Model (RCM) to capture the drift physics of the inner magnetosphere, whereby the fields and outer boundary conditions provided by the MHD model were used to drive the plasma drift mechanics of the ring current model [*Toffoletto et al.*, 2004]. This was a crucial first step in obtaining a fully self-consistent model of the inner and outer magnetosphere and ionosphere. This paper details the completion of the coupling strategy for LFM-RCM-MIX, where RCM-computed pressure and density are returned to the LFM and the MIX ionosphere model drives the convection pattern for both models.

[1]Department of Physics and Astronomy, Rice University, Houston, Texas, USA.
[2]High Altitude Observatory, National Center for Atmospheric Research, Boulder, Colorado, USA.
[3]Department of Physics and Astronomy, Dartmouth College, Hanover, New Hampshire, USA.
[4]Johns Hopkins University Applied Physics Laboratory, Johns Hopkins University, Laurel, Maryland, USA.

0148-0227/12/2011JA016979

1.2. Global MHD

[3] The equations of ideal single-fluid magnetohydrodynamics provide a self-consistent description of the Earth's magnetosphere and its interaction with the solar wind.

[4] Given a description of the solar wind, MHD models reproduce the large-scale features of the global electromagnetic field structure and plasma properties [*Fedder and Lyon*, 1987; *Raeder et al.*, 2001; *Wiltberger et al.*, 2005; *Ogino et al.*, 1985]. The Grand Unified Magnetosphere Ionosphere Coupling Simulation (GUMICS) [*Janhunen et al.*, 1996], the Block-Adaptive-Tree Solar wind Roe-Type Upwind Scheme (BATS-R-US) [*Powell et al.*, 1999; *Powell*, 1994; *Powell et al.*, 1995], and the Global Geospace Circulation Model (OpenGGCM) [*Raeder et al.*, 1998] are all implementations of global MHD, and vary with respect to implementation of the boundary conditions, grids, initial conditions, and even the formulation of the primary equations. The LFM [*Lyon et al.*, 2004] solves the conservative MHD equations on a static, deformed spherical mesh with axis along the Earth-Sun line, using the partial donor method [*Hain*, 1987]. The stretched spherical grid allows for high resolution to be placed near the Earth as well as at the bow shock.

1.3. Ring Current Models

[5] Single-fluid MHD models can represent the coupling of the magnetosphere to the solar wind and ionosphere. However, they only provide a rough approximation for the physics of the inner magnetosphere, where particle motion near Earth includes energy-dependent gradient-curvature drift. This causes the drift paths of earthward-traveling high-energy particles to be diverted westward (eastward) if the charge is positive (negative). Conversely, low-energy particles will first penetrate closer to Earth before the gradient-curvature drift is strong enough to divert them. The ring current is composed of both populations, which have sufficient current density to alter the global magnetic field. To model the inner magnetosphere, ring current (RC) models require a more detailed representation of plasma defined by magnetic moments and pitch angle. For example, the Fok Ring Current Model (FokRC) [*Fok et al.*, 1995] is a bounce-averaged kinetic ring current model that allows for non-isotropic pitch angle distributions, while the Comprehensive Ring Current Model (CRCM) [*Fok et al.*, 2001] uses a self-consistent electric field to evolve the FokRC distribution function. Similar to CRCM, the Ring Current-Atmosphere Interaction model (RAM) [*Jordanova et al.*, 1996] evolves energy and pitch angle distributions in time, using the Volland-Stern model for the electric potential [*Volland*, 1973; *Stern*, 1975]. More sophisticated versions of RAM include a self-consistent magnetic field [*Zaharia et al.*, 2006, 2010] that is in stable force balance with the RAM-computed pressures.

[6] The Rice Convection Model [*Harel et al.*, 1981; *Wolf*, 1983; *Toffoletto et al.*, 2003] formulation is similar to other RC models: it assumes that the plasma is slowly varying in time, that the plasma pressure is equilibrated along field lines, and waves are neglected. It further assumes an isotropic pitch angle distribution. The gradient in RCM's flux tube content can be related to ionospheric Birkeland currents via the Vasyliunas equation [*Vasyliunas*, 1970],and these currents drive RCM's ionospheric potential solver for low latitudes.

1.4. Ionospheric Models

[7] The ionosphere plays an important role in both global MHD and RC formulations. High conductivity in the ionosphere permits currents generated in the magnetosphere to close, and the presence of these currents in turn alters the conductance and the electric and magnetic fields over the whole system. MHD models must include a representation of the ionosphere in order to produce even basic global features due to the intrinsic coupling. Ionospheric conductivity may be solved in 3D [*Janhunen et al.*, 1996] or a height-integrated conductivity model may be used [*Ridley et al.*, 2004; *Raeder et al.*, 2001] to solve for the 2D electric potential. In the LFM, the 2D ionosphere solver MIX [*Merkin and Lyon*, 2010] serves as a replacement for LFM's original potential solver.

1.5. Coupled Models

[8] The ultimate goal of global modeling efforts is to construct a self-consistent first-principles model of the magnetosphere capable of accurately capturing both inner magnetospheric dynamics and outer magnetospheric morphology, such that the bow shock, plasma mantle, magnetotail, plasma sheet, and ring current are all accurately represented. In reality, all of these regions are coupled: sunward of a ring current enhancement, the day side magnetic field will increase, pushing the magnetopause boundary outward. Tailward reconnection produces earthward flows, and these flows can drive the ring current or enhance the shear flow in the flanks, both of which modify the Birkeland current distribution into the ionosphere. Ionospheric currents alter the electric field, which in turn modifies magnetospheric convection. A physics-based model typically solves a subset of the magnetospheric system. To incorporate missing physics from other regions, coupling between models is necessary.

[9] RC models can use Birkeland currents to alter the potential pattern for the inner magnetosphere such that the electric field is consistent with the plasma. However, in order for the system to be fully self-consistent, the magnetic field should also respond to any changes in the pressure. Several RC models have been augmented to solve for magnetic fields in force-balance with the plasma [*Toffoletto et al.*, 2003; *Lemon et al.*, 2004; *Zaharia et al.*, 2006; *Ebihara et al.*, 2008].

[10] The time dependence of the equilibrium-computed fields comes from the RC pressure distribution and the boundary conditions, for which there are empirical estimates. To provide more realistic outer boundary conditions, *Zaharia et al.* [2010] recently coupled the RAM-SCB boundary with BATS-R-US. Alternatively, several authors have used magnetic fields obtained from MHD simulations to drive RC simulations directly. A theoretical evaluation of the differences between the ring current formalism of the RCM and MHD can be found in work by *Heinemann and Wolf* [2001], who showed theoretically that the two can be made equivalent by extending MHD to include the effects of diamagnetic drifts and collisionless heat flux and also enforcing a Maxwellian distribution at every grid point and every time step in the RCM. However, they also

demonstrated that enforcing a Maxwellian in the RCM solution can drastically affect the evolution of pressures and densities. That conclusion was also confirmed using more realistic conditions by *Song et al.* [2008]. By coupling the RCM to the LFM, the effects of energy dependent drifts on MHD quantities, such as pressure and density, are incorporated into the LFM without the problems that accompany artificially enforcing a Maxwellian. In the "one-way" coupling paradigm, the flux tube volume is obtained from MHD field integrations and passed to the RC model, while MHD densities are used to populate the RC distribution function at the high-latitude outer boundary [*Hu et al.*, 2010; *Buzulukova et al.*, 2010]. The one-way coupling paradigm was initially used to drive RCM with LFM's magnetic field [*Toffoletto et al.*, 2004]. In order to make the plasma distribution consistent with both the electric and magnetic fields, a "two-way" coupling strategy is employed. In this scheme, the sum of pressures and densities over the RC distribution function is used to modify the single-fluid plasma in the MHD code, and the MHD model responds to the RC pressures and densities by modifying its own fields [*Hu et al.*, 2009; *De Zeeuw et al.*, 2004].

[11] This work details the two-way coupling strategy for LFM-RCM-MIX. In Section 2, we give a brief description of each model and its function within the larger coupling paradigm. Section 3 reports the response of the model to driving with idealized solar wind and ionosphere conditions by comparing with stand-alone MHD. We examine the effect of coupling on the ionosphere, MHD pressure, D_{st} signatures, and the distribution of flux tube entropy and mass content. In Section 4, we discuss the results in relation to flows of entropy and mass content, ring current pressure, and ionospheric shielding. Section 5 summarizes this work and presents further studies and improvements to the model.

2. Model Descriptions

[12] This section will provide a brief description of the models incorporated and details of the coupling procedure. In broad outline there are three components: The LFM global MHD model, the Rice Convection Model, and the MIX ionosphere solver. Their roles can be summarized as follows:

[13] The LFM provides a self-consistent model of the global magnetosphere, given the assumptions of single-fluid ideal MHD. The LFM does not include energy-dependent drifts in fluid velocity in the inner magnetosphere, and it requires an ionospheric model to set the inner boundary condition on velocity. Conversely, the RCM solves for the realistic energy-dependent drifts, but requires a magnetic field, electric potential, and plasma conditions specified on its outer boundary. Therefore, the LFM provides the RCM with a magnetic field model required for plasma convection and plasma conditions for the outer boundary of the RCM domain. In return, the RCM supplies the LFM with a more realistic ring current pressure and density distribution. Finally, both LFM and RCM receive an electric potential solution supplied by MIX, which accounts for both high and low-latitude convection. MIX solves for the ionospheric potential using the field-aligned current distribution obtained from the inner boundary of LFM.

2.1. LFM

[14] The LFM computes the 3D fields and plasma properties for all magnetospheric regions except for the inner magnetosphere and ionosphere. A description of the modeling framework of the LFM and its assumption of the plasma properties motivates the coupling scheme for LFM-RCM-MIX. A brief overview of the model is provided here, and more detailed information can be found in work by *Lyon et al.* [2004].

[15] The LFM solves the single-fluid MHD equations in semi-conservative form:

$$\frac{\partial \rho}{\partial t} = -\nabla \cdot (\rho \mathbf{v}) \tag{1}$$

$$\frac{\partial \rho \mathbf{v}}{\partial t} = -\nabla \cdot \left(\rho \mathbf{v}\mathbf{v} + \mathsf{I}\left(P + \frac{B^2}{2\mu_0}\right) - \frac{\mathbf{B}\mathbf{B}}{\mu_0} \right) \tag{2}$$

$$\frac{\partial e}{\partial t} = -\nabla \cdot ((e+P)\mathbf{v}) - \mathbf{v} \cdot \nabla \cdot \left(\mathsf{I}\frac{B^2}{2\mu_0} - \frac{\mathbf{B}\mathbf{B}}{\mu_0} \right) \tag{3}$$

$$\frac{\partial \mathbf{B}}{\partial t} = -\nabla \times \mathbf{E} \tag{4}$$

$$\mathbf{E} = -\mathbf{v} \times \mathbf{B} \tag{5}$$

$$\nabla \cdot \mathbf{B} = 0 \tag{6}$$

$$\mu_0 \mathbf{J} = \nabla \times \mathbf{B} \tag{7}$$

$$e = \frac{\rho v^2}{2} + \frac{P}{\gamma - 1} \tag{8}$$

where the usual variable definitions hold and $\gamma = 5/3$ [*Lyon et al.*, 2004]. Only plasma energy e is tracked, rather than the total energy; this avoids numerical problems in low-β regions where subtraction of magnetic field energy leads to errors in the plasma pressure. The electric field, **E**, is stored on mesh edges and the magnetic flux is stored on faces, while the magnetic field, **B**, density, ρ, pressure, P, and velocity, **v**, are stored at cell centers. The staggering of the fields maintains the divergence-free nature of **B** [*Yee*, 1966]. The finite volume method is used to update the conserved variables, using the total variance diminishing scheme to represent the fluxes [*Lyon et al.*, 2004]. The equations are solved on a stretched spherical grid with domain spanning from the near-Earth at 2.0 R_E to the distant tail (-300 R_E in GSM coordinates) and upstream of the bow shock (+30 R_E). For these results, we have run the LFM in "double" resolution ($53 \times 48 \times 64$), with cell volumes less than 0.2 R_E^3 at geosynchronous orbit.

[16] In the MHD approximation, the velocity distribution function is assumed to be Maxwellian in the plasma frame of reference. The bulk velocity perpendicular to the field is $\mathbf{E} \times \mathbf{B}/B^2$. This drift is independent of charge and energy. This assumption becomes invalid as the plasma approaches

regions of high gradient-curvature drift, which produces westward currents as the plasma differentially drifts depending on the constituent charge species and energy invariants. Therefore, the LFM plasma description is valid only outside of the regions where gradient-curvature drifts are large, and within that region LFM requires RCM to accurately model the plasma motion.

2.2. MIX

[17] The coupled magnetosphere-ionosphere interaction is managed by the MIX 2D electrostatic solver. The MIX computation is done on a spherical shell with the pole centered at the magnetic pole. At its basis is Ohm's law following from current continuity equation integrated over the ionospheric height. Combining these concepts,

$$\mathbf{E} = -\nabla_\perp \phi, \tag{9}$$

where $\nabla_\perp$ is the 2D gradient in the ionosphere, yields the following relation:

$$\nabla_\perp \cdot (\bar{\Sigma} \cdot \nabla_\perp \phi) = -j_\parallel \sin(I), \tag{10}$$

where $j_\parallel$ is the Birkeland current flowing into the ionosphere, I is the inclination angle of the magnetic field, and $\bar{\Sigma}$ is the conductance tensor. The conductance in the model can be fixed as in the results presented here, or it may include auroral and EUV effects [*Wiltberger et al.*, 2004]. Given a Birkeland current distribution over the ionosphere, specified conductances, and a choice of several low-latitude boundary conditions, MIX solves for the electric potential [*Merkin and Lyon*, 2010]. In the coupled model the LFM supplies the magnetic field, and the currents are obtained by numerical differentiation at the LFM inner boundary.

2.3. RCM

[18] The RCM treats the inner magnetospheric plasma as a bounce-averaged isotropic distribution, which allows the RCM to solve the system as a 2D advection problem on a mesh situated in the northern ionosphere. The plasma is divided into separate species (denoted by subscript i) and fluid channels (denoted by the subscript k), with 28 fluid channels for electrons and 62 for protons. Each k-channel is associated with an adiabatic invariant $\lambda_{i,k}$ given by

$$\lambda_{i,k} = W_{i,k} V(\mathbf{r})^{2/3} \tag{11}$$

in units of $\mathrm{eV}(\mathrm{R_E/nT})^{-2/3}$. $\lambda_{i,k}$ is a constant for each fluid and represents the total entropy per particle for that channel. Here, $W_{i,k}$[eV] is the average energy per particle and the flux tube volume $V(\mathbf{r})$ is calculated from a magnetic field model through the field line integral

$$V(\mathbf{r}) = \int_{\mathbf{r}} \frac{ds}{B}. \tag{12}$$

[19] The integration step length, **ds**, is measured in Earth radii and is parallel or anti-parallel to the magnetic field **B** [nT]. The integration limits span from the south to north ionospheres. Integration begins at positions **r** in the RCM grid, which is a fixed hemisphere above the northern ionosphere with radius 1 $\mathrm{R_E}$.

[20] The energy invariant formalism allows the RCM to follow the plasma for a given invariant $\lambda_{i,k}$, using the partial flux tube content $\eta_{i,k}$, representing the number of particles for channel k per unit magnetic flux [*Toffoletto et al.*, 2004]. The RCM evolves the spatial distribution of flux tube content by solving the advection equation

$$\left(\frac{\partial}{\partial t} + \mathbf{v}_D(\lambda_{i,k}, \mathbf{r}, t) \cdot \nabla\right) \eta_{i,k}(\mathbf{r}, t) = -\frac{\eta_{i,k}(\mathbf{r}, t)}{\tau_{i,k}(\mathbf{r}, t)} \tag{13}$$

where the LHS includes all energy-dependent drifts and the RHS includes losses due to electron precipitation or charge exchange, through the decay times $\tau_{i,k}$. Note that the decay times for charge-exchange are energy-dependent. Particle losses may be neglected without substantially changing the dynamics on timescales considered here, so that $\eta_{i,k}$ will be conserved along a path drifting with the plasma at velocity $\mathbf{v}_D$. By performing the RCM transport in the ionosphere the plasma motion can be characterized by an effective potential, $\Phi_{i,k}$, where the drift velocity is given by

$$\mathbf{v}_D = \frac{\mathbf{B}}{B^2} \times \nabla \Phi_{i,k}, \tag{14}$$

and

$$\Phi_{i,k} = \frac{\lambda_{i,k}}{q_i} V^{-2/3} + \phi. \tag{15}$$

[21] Inductive effects in the magnetosphere are accounted for through changes in the magnetic field model (i.e., through changes in V). For the results presented here, the electric potential from MIX is used. Since the drift velocity depends on the invariant $\lambda_{i,k}$ given in (11), the plasma will separate as each fluid moves along contours of constant $\Phi_{i,k}$.

[22] The RCM-computed flux tube content is related to the single-fluid MHD density and pressure. This compatibility is the basis of the coupling scheme used here, and results from careful construction of the RCM energy invariant domain. Suppressing the species index, the energy invariants are defined by channel centers λ_k and channel widths $\Delta\lambda_k$, given by

$$\Delta\lambda_k = \lambda_{k+1/2} - \lambda_{k-1/2}, \tag{16}$$

with

$$\lambda_{k\pm1/2} = \begin{cases} \dfrac{\lambda_k + \lambda_{k\pm1}}{2} & k_{\min} < k < k_{\max}, \\ 0 & k = k_{\min}, \\ 1.5\lambda_k - .5\lambda_{k-1} & k = k_{\max}. \end{cases} \tag{17}$$

[23] Thus, $\eta_{i,k}$ represents the total number of particles within the channel centered on λ_k, and a direct integration over the individual channels yields the total density ρ_i, pressure P_i and entropy S_i for species with mass m_i,

$$\rho_i = \left(1.5694 \times 10^{-16}\right) \frac{m_i}{m_p} \frac{1}{V} \sum_k \eta_{i,k} \tag{18}$$

$$P_i = \left(1.674 \times 10^{-35}\right) V^{-5/3} \sum_k \lambda_k \eta_{i,k} \tag{19}$$

$$S_i = P_i V^{5/3} \tag{20}$$

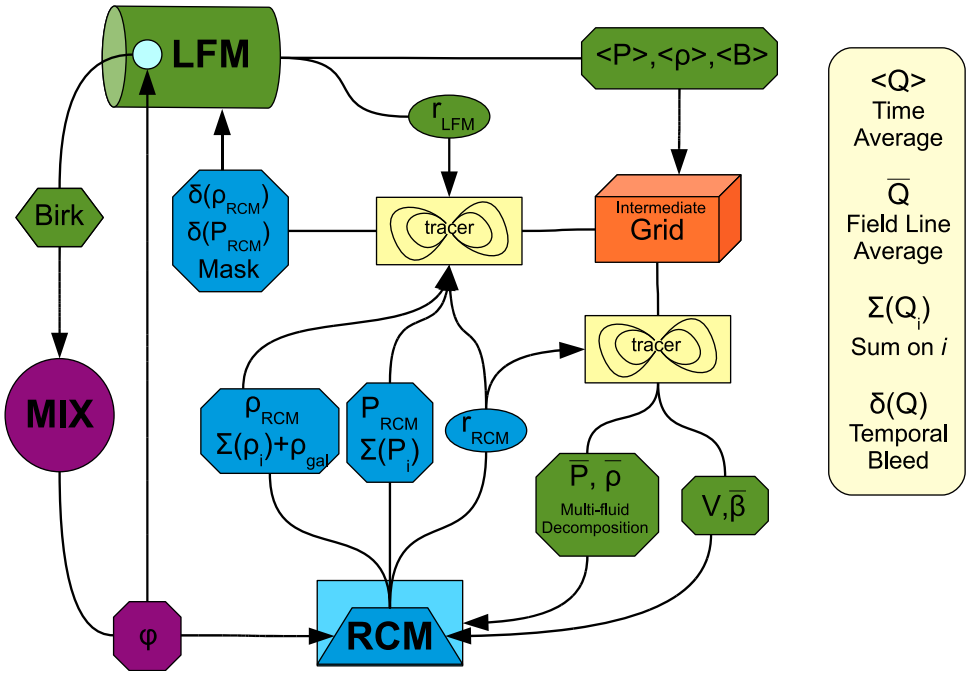

Figure 1. Flow diagram for LFM-RCM-MIX exchanges. Green, blue, and purple polygons represent variables sent from LFM, RCM, and MIX, respectively. Arrow heads indicate the direction of information exchange. The light blue circle in the LFM represents the LFM inner boundary, while the light blue region around RCM represents the RCM outer boundary.

where V is the flux tube volume, the sum is over the fluid index k, and m_i/m_p is the ratio of the species and proton masses.

2.4. Coupling Algorithm

[24] The model is part of the Center for Integrated Space Weather Modeling (CISM) [*Goodrich et al.*, 2004] simulation program, which seeks to develop a complete Sun-to-Earth model from first-principles. In the CISM architecture, the constituent models operate as separate executables and information is exchanged between them using the Intercomm runtime library [*Lee and Sussman*, 2004] together with Overture [*Brown et al.*, 1997], which manages interpolation between overset grids and is built upon the P++ parallel array class library. In general, the CISM approach attempts to minimize changes to the contributing models.

[25] In the LFM-RCM-MIX model, information exchange occurs on a regular schedule. Figure 1 illustrates the coupling algorithm. Variables are color-coded according to the model that produces them, while arrows point in the direction of information exchange. The LFM, represented by the green cylinder, transmits currents to MIX and plasma properties to RCM, as denoted by the green boxes. MIX transmits the electrostatic potential (purple) to both the LFM and RCM. The RCM returns plasma properties (blue) to the LFM, via field line traces. The rightmost key defines operations for time averages, field line averages, summations, and bleeding scheme used in the transfer. The tracer boxes depict field line integration, utilizing an intermediate grid (the orange box). Each portion of the diagram is explained in the following subsections.

2.4.1. Coupling to MIX

[26] LFM and RCM require the potential solution provided by MIX, while MIX requires a Birkeland current distribution. Active conductances are disabled in these test runs, though a data path exists for LFM quantities affecting conductances, e.g. density and sound speed, to be sent to MIX. Exchanges with MIX are depicted at the leftmost part of Figure 1. LFM Birkeland currents are mapped along a dipole field from the LFM inner boundary (2.2 R_E) to the height of the MIX ionosphere. From current continuity, the relative increase in current density is proportional to the increase in the magnetic field strength, such that

$$j_{\|ion} = \frac{B_{ion}}{B_m} j_{\|m} \tag{21}$$

where $j_{\|ion}$ represents the ionospheric current parallel to the magnetic field, $j_{\|m}$ the parallel current at the inner boundary, and B_{ion}/B_m the ratio of the magnetic field strengths at the ionosphere and inner boundary, respectively. The resulting currents are then interpolated onto the MIX domain, where they are used to solve for the potential in equation (10). The potential pattern obtained from MIX is returned to the LFM inner boundary to drive magnetospheric convection. The LFM-MIX exchange occurs every 10 s in simulation time.

[27] After a preconditioning interval, which allows the model to develop a magnetosphere from its initial condition, coupling to the RCM is turned on (t = 0 for all the results shown here). The potential pattern obtained from MIX is interpolated onto the RCM's ionospheric grid, where it is used in the calculation of gradient and curvature drift. An option exists to return average energy, energy flux, and Birkeland currents from RCM to MIX, where the RCM currents are obtained through the Vasyliunas equation [*Wolf*, 1983]. However, this option is disabled in these runs.

Effectively, the feedback of RCM pressures to the ionosphere is mediated by the LFM-RCM coupling.

2.4.2. LFM to RCM Transfer

[28] The LFM solves for the time-dependent electric and magnetic fields and plasma, with adjustments to ring current pressure and density supplied by RCM. For the first exchange, the LFM updates the RCM plasma distribution over the entire RCM domain, assuming a Maxwellian energy distribution. For all subsequent exchanges, only the RCM outer boundary (light blue box enclosing RCM in Figure 1) is updated with LFM plasma. The exchange of information from LFM to RCM is shown in Figure 1, moving clockwise away from LFM.

[29] The time averages of LFM pressure, density, and magnetic field are computed over a 1-minute exchange time (see Appendix A). Since the MHD code is constantly evolving between exchanges, the 1-minute exchange time serves as a compromise between speed and accuracy: more frequent exchanges may produce more accurate coupling with respect to capturing the instantaneous LFM, but would become computationally expensive. Numerical experiments indicate the results are not sensitive to exchange times in the 1-minute range. This also reduces any high-temporal variation in LFM to keep consistency with the RCM assumption that waves are not present.

[30] The minute-averages of density, pressure, and magnetic field are interpolated onto an intermediate grid. The grid is a regular Cartesian mesh and has higher average resolution than the LFM, such that the LFM results are captured accurately. The grid spans the domain $(-30, 15)R_E$ along the Earth-Sun line and ± 20 R_E in y and z. A search in this intermediate grid is straight-forward compared to a similar search in the LFM mesh, so this simplifies the field line tracer and improves overall speed even when including the interpolation time. Field line-averaged pressure and density are obtained from traces initiated from positions in RCM's ionospheric grid ($\mathbf{r}_{RCM}$ in the figure), given by

$$\langle \bar{P}, \bar{\rho} \rangle = \frac{\int \langle P \rangle, \langle \rho \rangle ds/B}{\int ds/B}, \tag{22}$$

where the denominator is the flux tube volume V used in equation (15) for the RCM effective potential.

[31] Once the time-averaged field-integrated pressures and densities are specified at the RCM's ionospheric grid, these quantities are put in terms of the RCM variable $\eta_{i,k}$ as a function of the energy invariant $\lambda_{i,k}$ introduced in section 2.3. Appendix B describes the decomposition of LFM plasma into RCM electron and proton distribution functions.

2.4.3. Setting the RCM Boundary Location

[32] The RCM domain consists of a static 2D grid in the ionosphere and its magnetic projection onto the equatorial plane. The former is spherical with minimum latitude of 10°, and the latter is determined by magnetic field mapping onto the equatorial plane. If an RCM foot point lies along an open field line or intersects the equatorial plane outside a specified elliptical boundary, then it is removed from the modeling domain. The location of the RCM outer boundary ultimately determines where gradient-curvature drift dynamics are enforced.

[33] Under conditions of steady driving with a southward IMF the above boundary specification eventually resulted in the LFM producing large radial flows near the outer edge of the RCM modeling region, where the equatorial plasma-β became much larger than one. The reasons for these flows are likely due to several factors, including insufficient resolution in the MHD code to balance the large pressure gradients in the inner magnetosphere produced by the RCM. In the case where the plasma-β is large, static equilibrium requires that the pressure gradient be balanced by a large field-line curvature. If the LFM cannot represent such curvature due to grid resolution, then a numerically driven flow will likely be produced. Numerical experiments with lower/higher resolution versions of the LFM resulted in the appearance of these flows at earlier/later times, which is consistent with the resolution playing some role in the formation of these flows. Additionally, these flows could be a manifestation of a physical instability [e.g., *Pu et al.*, 1997].

[34] To prevent the occurrence of non-physical flows, various options for setting the RCM boundary were explored. For the results in this paper a criterion was adopted that restricts the RCM boundary based on flux tube average plasma-β, defined by

$$\bar{\beta} \equiv \frac{\int 2\mu_0 p ds/B^3}{\int ds/B} \tag{23}$$

where the averaging is weighted by $1/B$. This weighting tends to favor the equatorial region, where the field is weakest. For the cases presented here, $\bar{\beta} \leq 1$ was used as the criteria for defining the RCM coupling region. While other criteria for choosing the RCM boundary are also possible, this criterion produced the most stable results while still allowing the RCM to operate in a region that encompassed the peak of the ring current pressure. The choice of a flux tube averaged β restriction has the additional advantage of restricting the RCM modeling region to where its assumption of quasi-static slow flow is valid. Recent work of *Wolf et al.* [2012a, 2012b] comparing the RCM's quasi-static slow flow approximation to MHD using a 1-dimensional filament code found that under conditions where the equatorial plasma-β became larger than one, the MHD code would often produce wave-like solutions that the RCM does not represent. The choice of boundary is a compromise: it allows the LFM to govern the regions of fast flows but removes much of the potentially important drift physics that the RCM would otherwise capture. During southward IMF, the RCM boundary typically lies within 6 R_E.

2.4.4. RCM to LFM Transfer

[35] The transfer of information from RCM to LFM is shown in Figure 1, moving from the bottom to the top of the diagram, beginning with RCM. After the RCM has run for a set time (Δt = 60s), the sum over the RCM partial pressures and densities is obtained using equations (18) and (19). In addition, the RCM density is modified with the addition of a fit to the static plasmasphere model of *Gallagher et al.* [2000] (see Appendix C). As a temporary substitute for a full treatment of the plasmasphere, this has the effect of providing a cold component of plasma to the inner

magnetosphere. In future versions of the code a more realistic plasmasphere that incorporates the effects of the electric field and corotation will be included.

[36] The final density and pressure are transferred to the LFM by tracing field lines from points in the 3D LFM domain, using the magnetic field stored on the regular intermediate grid. The intersection of each trace with the RCM ionospheric grid is used to interpolate the local RCM pressure and density. At this stage, a mask variable specifies whether an LFM grid point maps into the RCM domain, which determines if the LFM density and pressure should be modified. These RCM quantities do not immediately replace the LFM variables, but are instead bled into LFM over the exchange time. This bleed scheme prevents discontinuities from forming at the boundary of RCM. The modification is made to the LFM sound speed c_{LFM}, using

$$c_{LFM}(t) = c_{LFM}(t) + (c_{RCM} - c_{LFM}(t))\frac{dt}{\Delta t}R, \qquad (24)$$

where c_{RCM} is the RCM sound speed, $dt/\Delta t$ is the ratio of the current LFM time step to the exchange time interval, and R is a coupling constant that controls the strength of the coupling. If $R = 0$, the LFM variables are unchanged and coupling is effectively turned off. For the runs shown here, we set $R = 1$. A similar algorithm to equation (24) is used to adjust the LFM density.

3. Model Results

3.1. Description of Run Setup

[37] With appropriate solar wind conditions, the coupled magnetosphere-ionosphere-ring current simulation should produce several features of storm-time dynamics. A ring current pressure enhancement should occur, in addition to ionospheric shielding and changes in the magnetopause location. Without the test runs performed here, it would be difficult to predict exactly how the system will respond, given the various competing physical processes at work. For example, Birkeland currents would modify the potential of the ionosphere, changing the global convection electric field, while the change in convection pattern in turn alters the Birkeland current.

[38] LFM-RCM-MIX was run in two modes: coupled and uncoupled. In the coupled runs, the full machinery of the coupling scheme described in 2.4 was used. For the uncoupled runs, the bleed rate R in section 2.4.4 was set to zero. In this mode, RCM densities and pressures do not modify the LFM parameters. The uncoupled mode will be used to determine the overall effect the RCM has when combined with LFM-MIX.

[39] The coupled and uncoupled models were tested with two idealized solar wind and ionospheric conditions. A constant solar wind velocity of $v_x = 400$ km/s and a constant pressure and density corresponding to a sonic Mach number of 10 were used, together with a fixed ionospheric conductance of 10 S. The only change in the solar wind was from the time-varying interplanetary magnetic field of $B_z = \pm 5$ nT. The two runs investigated used similar IMF conditions. In the case of the "S IMF" runs, IMF B_z was predominantly southward, except for a northward interval from 02:00–04:00 UT. For the "SN IMF" runs, the same time dependence as the S IMF case was used until the second southward turning, after which the B_z direction switched every 3 hours.

3.2. Overview of Simulation Results

[40] Figure 2 compares the basic response of the coupled (LFM-RCM-MIX) and uncoupled (LFM-MIX) S IMF and SN IMF runs. Figure 2a shows the integrated Birkeland current into the northern polar cap (FAC_N). In both coupled and uncoupled runs, the first 2 hours of southward IMF is an initialization phase used only to prime the magnetosphere. LFM-RCM-MIX consistently produces stronger Birkeland currents than LFM-MIX, nearly a factor of 1.5 higher beginning at 08:00 UT for the S IMF runs. An analysis of the Birkeland currents revealed that Region-2 currents were 2.5× higher in the coupled S IMF run when compared to the uncoupled run over the 08:00–16:00 UT period, while the increase in the region-1 currents was 20% for the same interval.

[41] Figure 2b shows the cross polar cap potential drop, which is obtained from the difference of the minimum and maximum potential in MIX. After the southward turning at 04:00 UT, all four runs reach an initial peak of 80 kV at 04:40 UT. After this initial peak the potential decreases during the next hour for all the runs while the Birkeland currents stabilize. At 05:30 UT all four runs show strong variations in potential that correspond to abrupt changes in Birkeland current, marking the beginning of substorm onset. The onset of the rapid variations in Birkeland current occurs earlier in the uncoupled runs, and a corresponding second potential peak occurs earlier, at 05:40 UT in the uncoupled runs while at 06:30 UT in the coupled runs. For the uncoupled S IMF case, after 07:00 UT the polar cap potential remains near 90 kV and does not exceed 100 kV for the remainder of the run, while in the coupled run the peak potential is 110 kV (at 08:30 UT) and oscillates around 100 kV for the remainder of the run. 10 kV oscillations occurring in coupled and uncoupled runs have a period of about 10 min. These reflect Birkeland current oscillations with the same period, but they persist for the duration of the coupled S IMF run, with minima close to a steady potential obtained by the uncoupled S IMF run. In the SN IMF run, the polar cap potential and Birkeland currents reach nearly the same values as the long duration runs, so the northward interlude did not affect the long-term behavior, at least on the global scale. Compared to the magnitude of the polar cap potentials, the potential oscillations are relatively small. Note that the polar cap potential produced by the various runs are in the expected range for these solar wind conditions: using the empirical estimate of *Boyle et al.* [1997] yields a polar cap potential of 76 kV. However, the potential obtained from the model is highly dependent on the ionospheric conductance.

[42] Figure 2c shows the response of the magnetic field through D_{st}, which is approximated by averaging the magnetic field perturbation near the inner boundary of the LFM. The initial value of 40 nT D_{st} does not bear much physical significance, since it depends largely on the startup configuration of LFM. However, comparing the relative strength between the runs is an indication of the large-scale changes in the magnetic field close to Earth. Observing the response of the S IMF coupled and uncoupled runs (blue and red

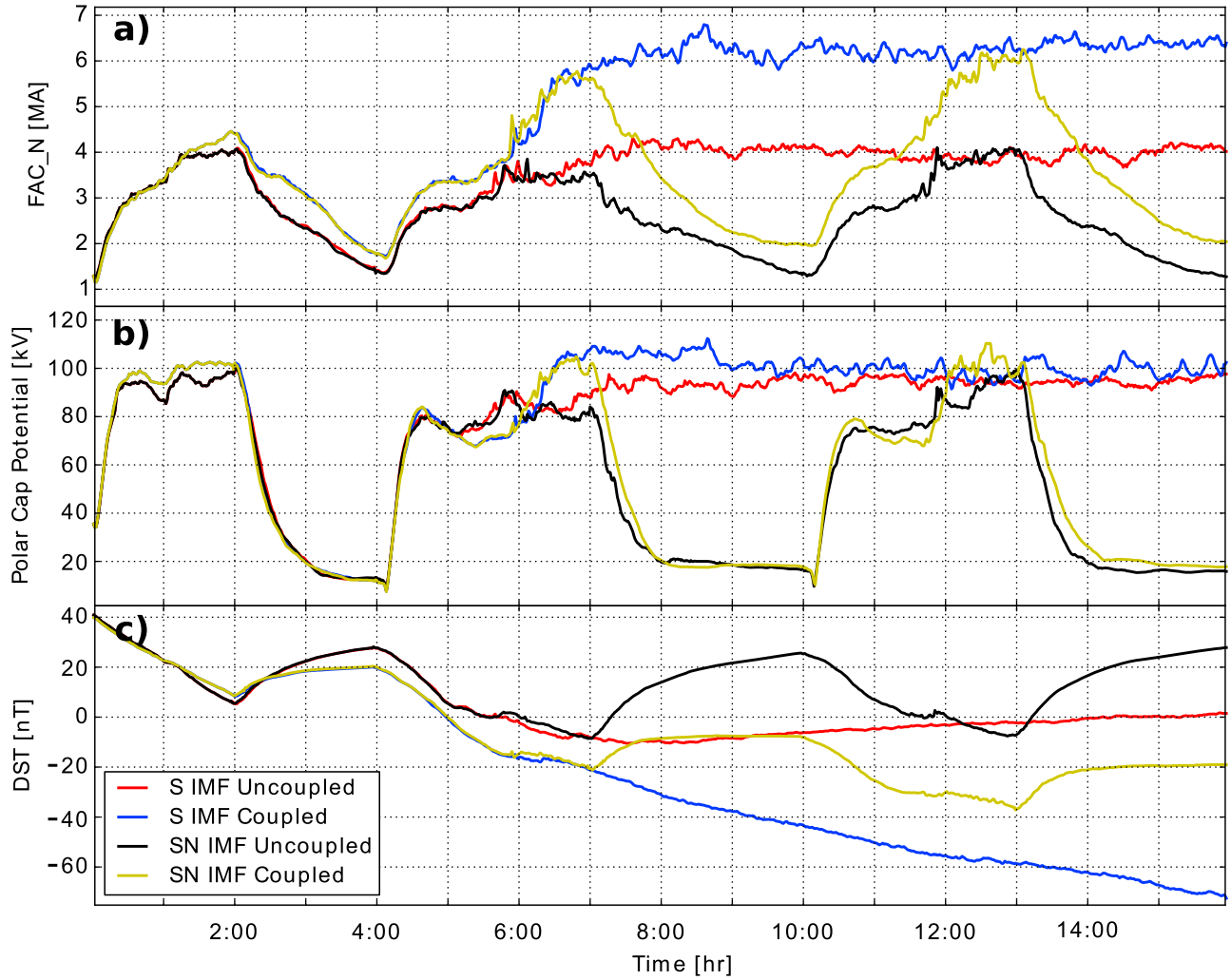

Figure 2. (a) Field-aligned current in MIX for coupled (blue) and uncoupled (red) S IMF runs; coupled (yellow) and uncoupled (black) SN IMF runs are also shown. (b) Polar cap potential drop in MIX. (c) D_{st} measured at inner boundary of LFM.

curves, respectively) shows that the presence of RCM pressures produces a more negative response in the magnetic field perturbation. This effect becomes noticeable in the period from 0200–0700 UT, where the D_{st} signatures correlate strongly. Here, the uncoupled run begins to diverge from the coupled case, with a 10 nT gap just prior to the southward turning at 0400 UT. After southward turning, the field decreases for both runs. However, at 0700 UT the uncoupled run minimizes and begins a slow recovery for the duration of the run, while in the coupled run the magnetic field continually decreases. This difference is reflected in the SN IMF coupled and uncoupled runs (yellow and black curves, respectively): in the uncoupled run the D_{st} tends to reach extrema near the same values, while the coupled run reaches successively lower extrema. Note that the coupled SN IMF run approaches the uncoupled S IMF run from 0730 to 1000 UT. This is most likely coincidental, since the next northward interval does not return the coupled run to the same value. Further investigation found that for the coupled S IMF run, the D_{st} decreased at a continuous rate during a 40 hour period of constant southward IMF. However, when RCM particle losses due to charge exchange and electron precipitation were enabled, D_{st} reached a minimum of −40 nT after 10–15 hours.

[43] The D_{st} signatures indicate that LFM plasma pressure should be significantly larger in the coupled cases in order to significantly reduce the average magnetic field in the inner magnetosphere. Figure 3 examines the influence the RCM has on the LFM pressure, 12 hours after the first southward turning. LFM equatorial pressure is shown with the Sun to the left. The pressure enhancement closest to the Sun on the day side indicates the location of the bow shock, the inner edge of the enhancement is a proxy for the magnetopause, and the magnetosheath lies between the two. Figures 3a and 3b compare results for the uncoupled and coupled S IMF runs. In the uncoupled run, a diffuse build-up of low pressure (<3 nPa) fills the nightside region close to the Earth and peaks at the inner boundary of the LFM. On the day side there is a wedge of depleted pressure spanning from 0800 to 1600 local time; the convection potential prevents the plasma from filling this region. In Figure 3b, when the RCM is included, a strong partial ring current develops. This is signified by a high pressure region on the night side that peaks at over 60 nPa at a radial distance of 4 R_E.

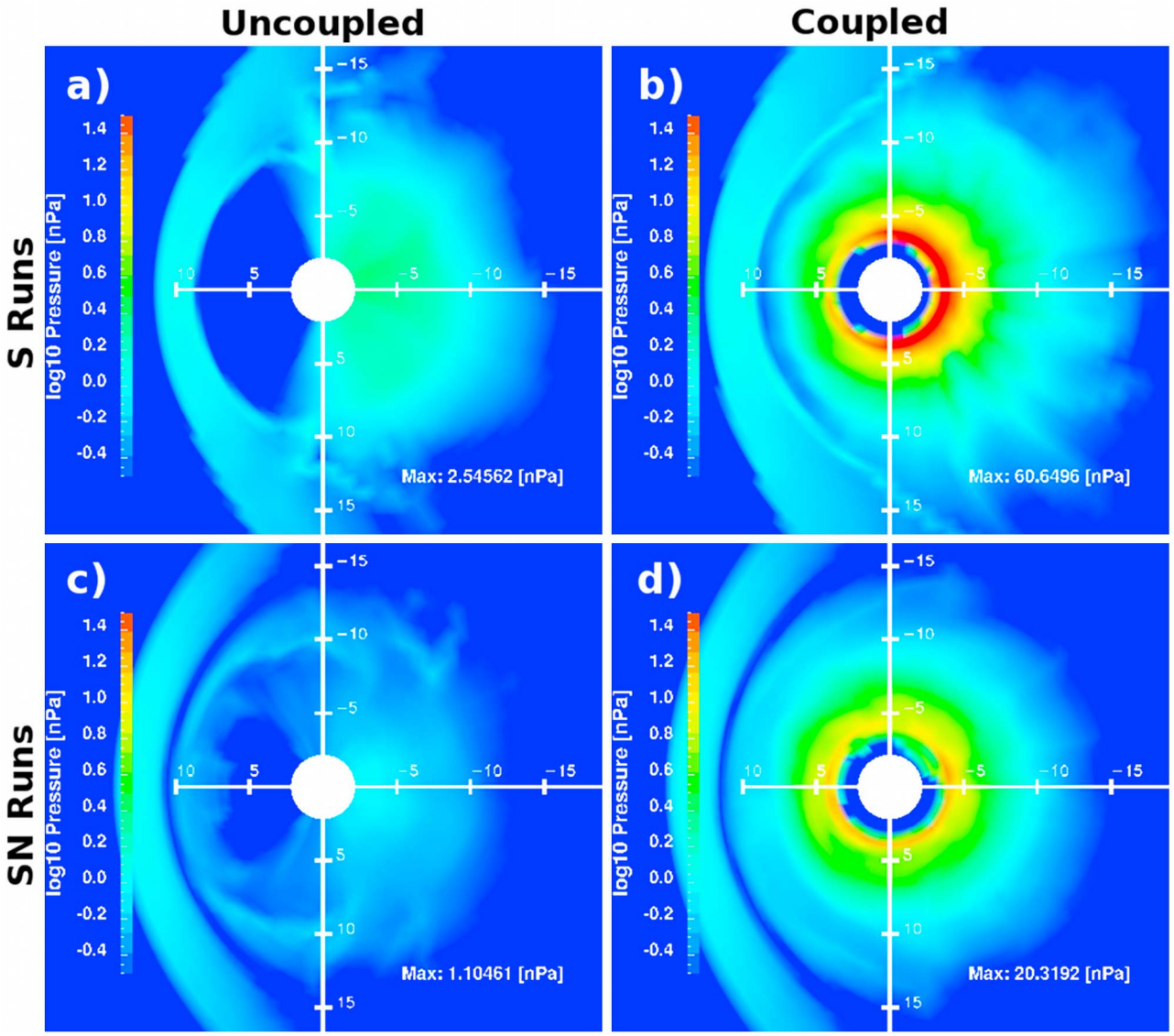

Figure 3. Buildup of ring current in the (a and c) uncoupled vs (b and d) coupled runs for S IMF (Figures 3a and 3b) and SN IMF (Figures 3c and 3d). The view is from above the north pole with the sun to the left at 1600 UT. Peak ring current pressures are listed for each.

[44] Figure 3c shows the uncoupled LFM pressure for the SN run 3 hours after the last northward turning. Some of the dayside wedge between 6 and 10 R_E has been filled in with diffuse pressure, and there is a sharp drop in pressure at the subsolar point at 11 R_E. This is the point at which the magnetic pressure dominates, holding off the sheath flow while the northward IMF prevents reconnection from mixing magnetosheath and magnetospheric plasma. In contrast, Figure 3d shows the pressure in the coupled run is again higher by an order of magnitude. The ring current has become azimuthally symmetric after 3 hours of northward IMF. However, the trapped ring current population produces a pressure a factor of 3 less than the S IMF coupled run, and this is likely due to the SN IMF run experiencing shorter periods of southward IMF.

[45] A detailed study of the pressures shown in Figure 3 revealed that the peak pressures are at $\mathbf{r} \approx 4$ R_E for the coupled runs, with the peak favoring the day side for the SN IMF run by 2× the night side pressure. Conversely, the S IMF run has a peak 5× higher on the night side than the day side. In general, the peak pressures are not aligned with the noon-midnight meridian.

3.3. Ionospheric Response

[46] One of the characteristics of RC models is the development of strong region-2 Birkeland currents, which have an impact on the electric field at low latitudes. In particular, during steady convection, such as when the IMF B_z is southward, the region-2 currents would be expected to shield the low-latitude electric field [*Wolf and Spiro*, 1983]. Figure 4 shows the polar cap potential with 5 kV potential spacing and Birkeland currents for the uncoupled (left) and coupled (right) S IMF runs. Figures 4c and 4d are the instantaneous values and Figures 4a and 4b show the same

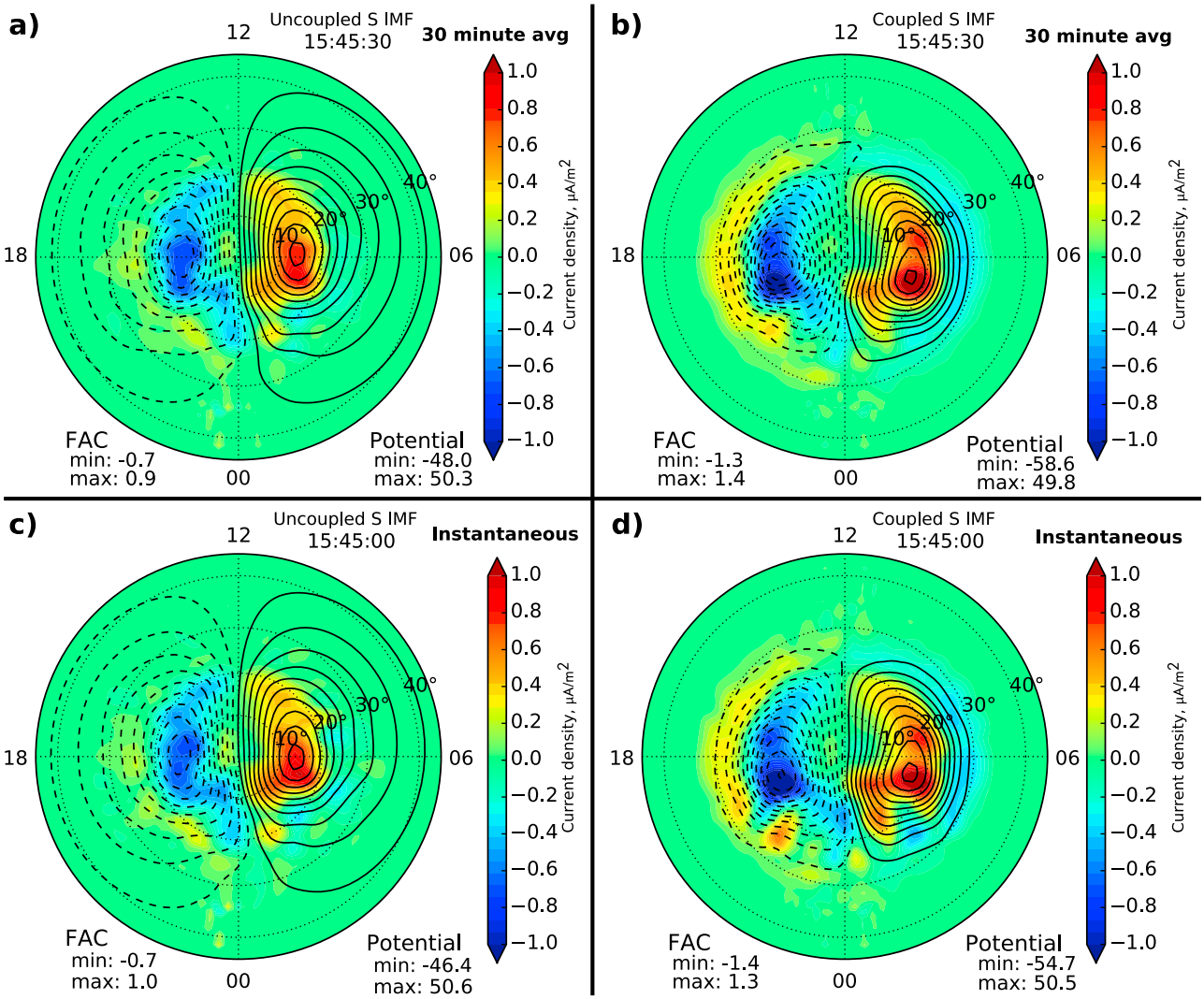

Figure 4. Thirty-minute averaged Polar Cap Potential (PCP) with 5 kV spacing and 30-minute averaged Birkeland currents for (a) uncoupled and (b) coupled S-IMF run. The uncoupled exhibits some shielding, indicated by a drop in electric field intensity as seen from the more widely spaced equipotentials. This shielding is much more pronounced in the coupled run. Region-2 currents are significantly stronger in the low-latitude region for the coupled run. (c and d) Instantaneous views of the ionospheric patterns are shown.

quantities but averaged over 30 min around the time in the instantaneous values. Both the coupled runs exhibit strong Birkeland currents and shielding, while the averaged plots resemble more closely the traditional *Iijima and Potemra* [1978] Birkeland current patterns. There are instantaneous features in the Birkeland current that are not seen in the time-averaged plot, such as the intensification at 25° colatitude, 2200 LT. These transient patterns occur more frequently in the coupled runs; they tend to propagate from high to low latitudes on the night side, followed by motion toward dawn (if the enhancement began in the post-midnight sector) or dusk (for the pre-midnight sector). The transient patterns then merge with the extended Region-2 system on the day side.

[47] Figure 5 shows polar cap potential with 5 kV potential spacing and Birkeland currents for the uncoupled (Figure 5, left) and coupled (Figure 5, right) SN IMF runs, 40 min after northward turning. The midlatitude potential peaks at this time, with opposite polarity from the convection electric field. This "overshielding" response gradually decays over the next hour. Figure 6 shows undershielding for the SN IMF uncoupled run (Figure 6, left). At this time the ring current has yet to fully symmetrize and shielding is reduced when compared to the coupled run (Figure 6, right). In this case, the convection electric field is still active in the inner magnetosphere prior to the build-up of Region-2 currents.

3.4. Magnetic Field at Geosynchronous Orbit

[48] From the basic global responses seen in Figure 2 the magnetic field in LFM is reduced in response to the ring current pressures imposed by RCM. Figures 7 and 8 examine the magnetic field in more detail: the z-component of the magnetic field at geosynchronous orbit (6.6 R_E) is plotted for several local times, spanning 1800 to 0600 LT across the

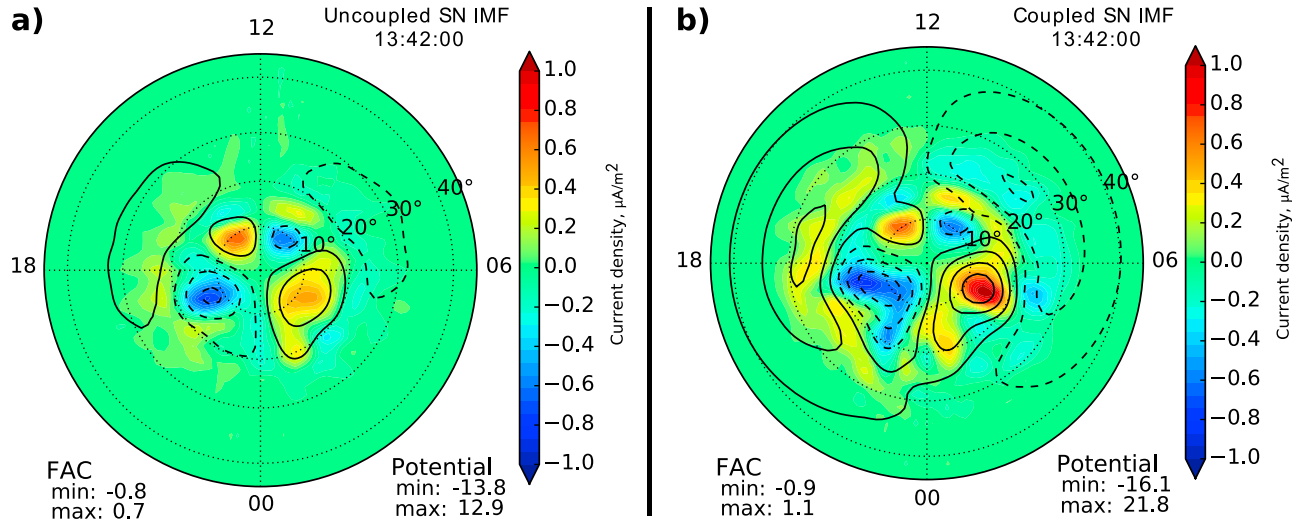

Figure 5. Polar cap potential with dashed (negative) and solid (positive) potential contours spaced at 5 kV, together with Birkeland currents for the (a) uncoupled and (b) coupled SN IMF run, 40 min after northward turning. The presence of stronger Region-2 currents produces "over-shielding" in the coupled run, signified by a reversal of the electric field.

night side. In the uncoupled runs, the magnetic field is overall larger than in the coupled cases, except for periods where the coupled run oscillations briefly exceed the relatively steady values seen in the uncoupled runs (the uncoupled oscillations are very small, 10 nT in the strongest case). This affirms the idea that the RCM ring current has reduced the overall strength of the magnetic field on the night side. The highest variability occurs for the S IMF coupled run (blue curves of Figure 7) with oscillations that are sharply peaked for dawn and dusk and reduce in amplitude closer to midnight local time. These oscillations begin just before 0600 UT, which is the time of substorm onset seen in the Birkeland current signature of Figure 2. The coupled SN IMF run (Figure 8, yellow curve) shows similar behavior to the S IMF run, but only when the IMF is southward.

3.5. Entropy Analysis

[49] In section 3.4, magnetic field oscillations were observed at geosynchronous orbit in LFM on the night side, while in section 3.3 transient Birkeland currents were observed in MIX at low-latitudes, propagating toward the dawn and dusk flanks and merging with the Region-2 current system. Several authors have shown that flux tube entropy and density are useful parameterizations for interpreting the features of storm time injection [*Zhang et al.*, 2008; *Birn et al.*, 2009]. Analysis of the flux tube entropy and density is a useful diagnostic in understanding these oscillations.

[50] The local entropy and particle density should be conserved along drift paths in MHD. From the frozen-in condition, it follows that the total entropy and particle number per unit magnetic flux should also be conserved

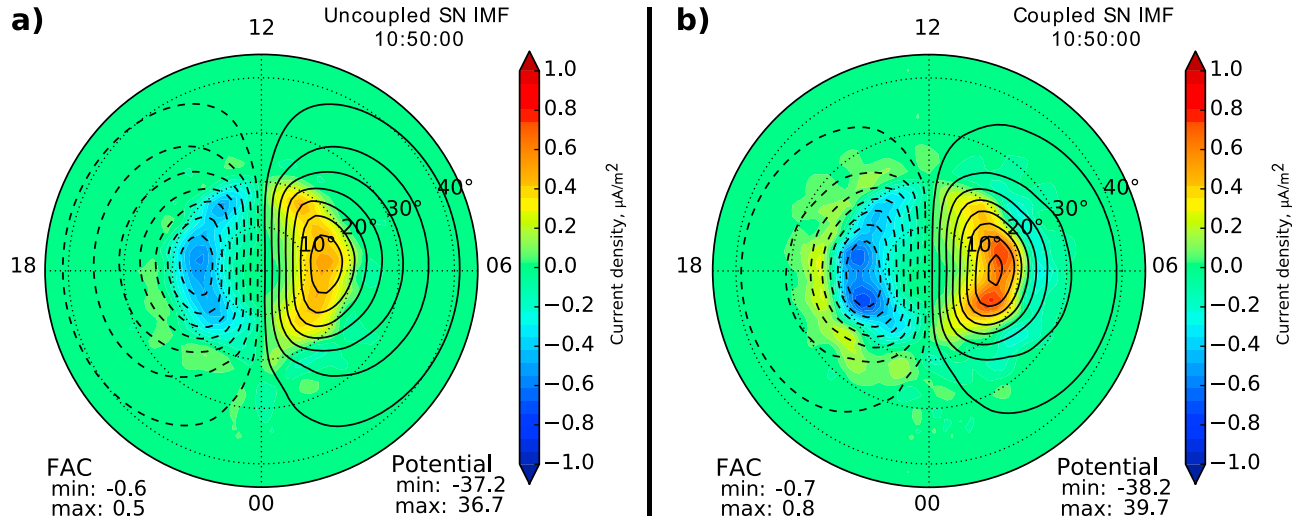

Figure 6. Same parameters as Figure 5 for (a) uncoupled and (b) coupled NSNS runs, 50 min after southward turning. Characteristic "under shielding" is signified by penetrating electric fields at low latitudes. Under-shielding is more pronounced in the uncoupled run.

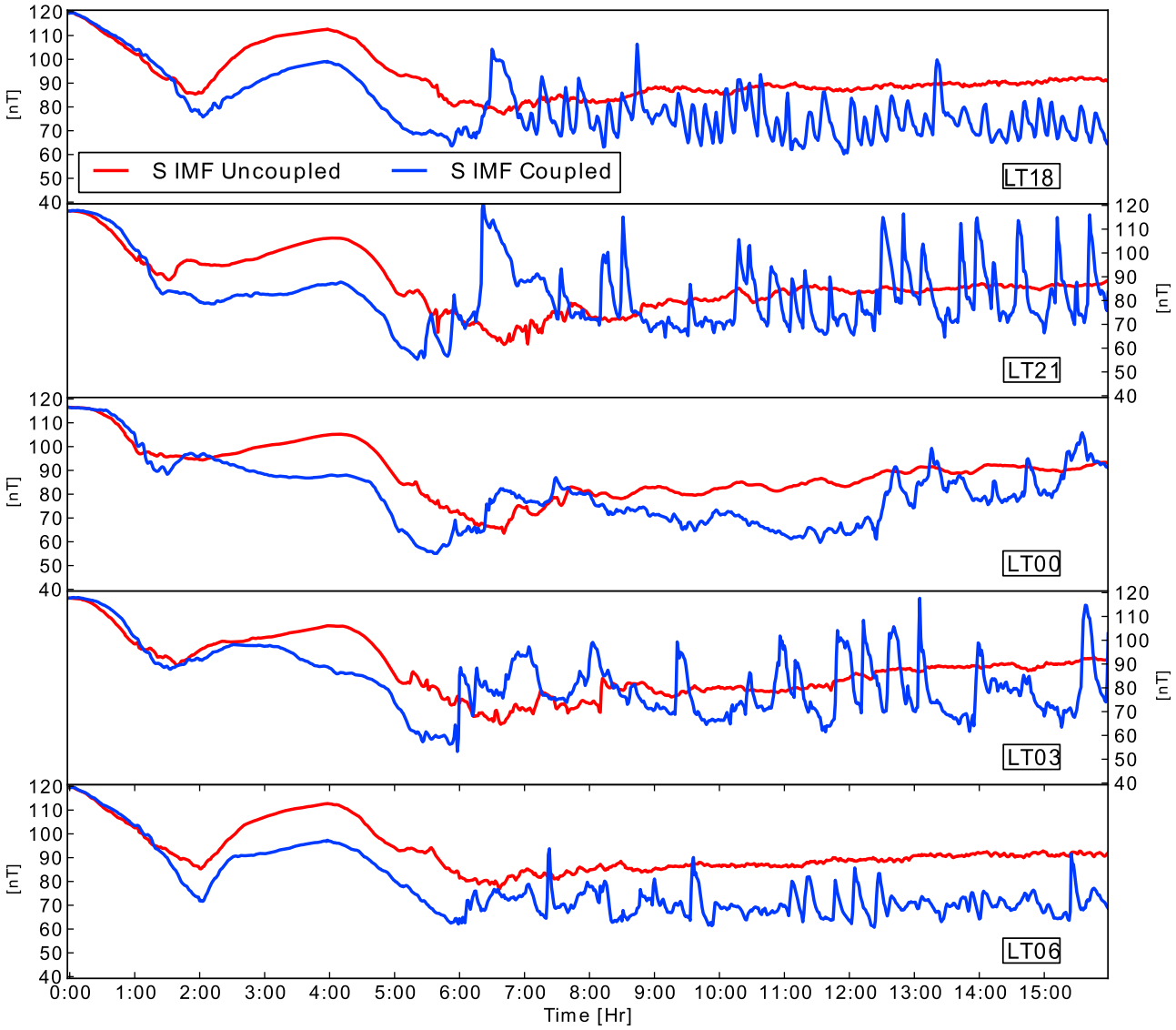

Figure 7. Response of magnetic field at geosynchronous orbit for coupled (blue) and uncoupled (red) S IMF runs. B_z is sampled on the night side at local times ranging from (top) dusk to (bottom) dawn.

[*Wolf et al.*, 2009; *Birn et al.*, 2009], so these parameters can be used to track the motion of plasma in the LFM. For the inner magnetosphere, the physics is more complex: when particle losses are disabled, the RCM will conserve both the entropy per particle and the number of particles per unit magnetic flux through the energy invariant λ. However, the drift paths of each fluid will depend on the strength of the gradient-curvature drift, which increases with λ and produces east-west motion. This results in two effects unique to the coupled code. According to the RCM formulation, plasma in low-λ channels is allowed to propagate closer to the Earth than in high-λ channels. The second effect is due to the relative motions of plasma in different λ-channels within the RCM. Even though the entropy in each channel is conserved, the drift paths of individual fluids can cross. Therefore, the sum of flux tube entropy and mass content over all channels will not be conserved locally. The result is a diffusive effect which will dominate closer to Earth, where flux tube volume is small. This effect will not contradict with the LFM description far from Earth where the flux tube volume is large, since each plasma species will drift together at the $\mathbf{E} \times \mathbf{B}$ velocity. Summarizing, in the coupled code entropy and mass content should be conserved far from Earth where LFM operates. If a low-entropy bubble moves into the inner magnetosphere, it should diffuse as the constituent plasma species separate in RCM.

[51] For the results below, all field line integrations were performed on the intermediate grid described in section 2.4.2. (Animations for each figure are available in the auxiliary material.)[1] The field line tracer used for visualization occasionally terminates prematurely before reaching the inner boundary, causing empty squares to appear in the figures.

[1]Auxiliary materials are available in the HTML. doi:10.1029/2011JA016979.

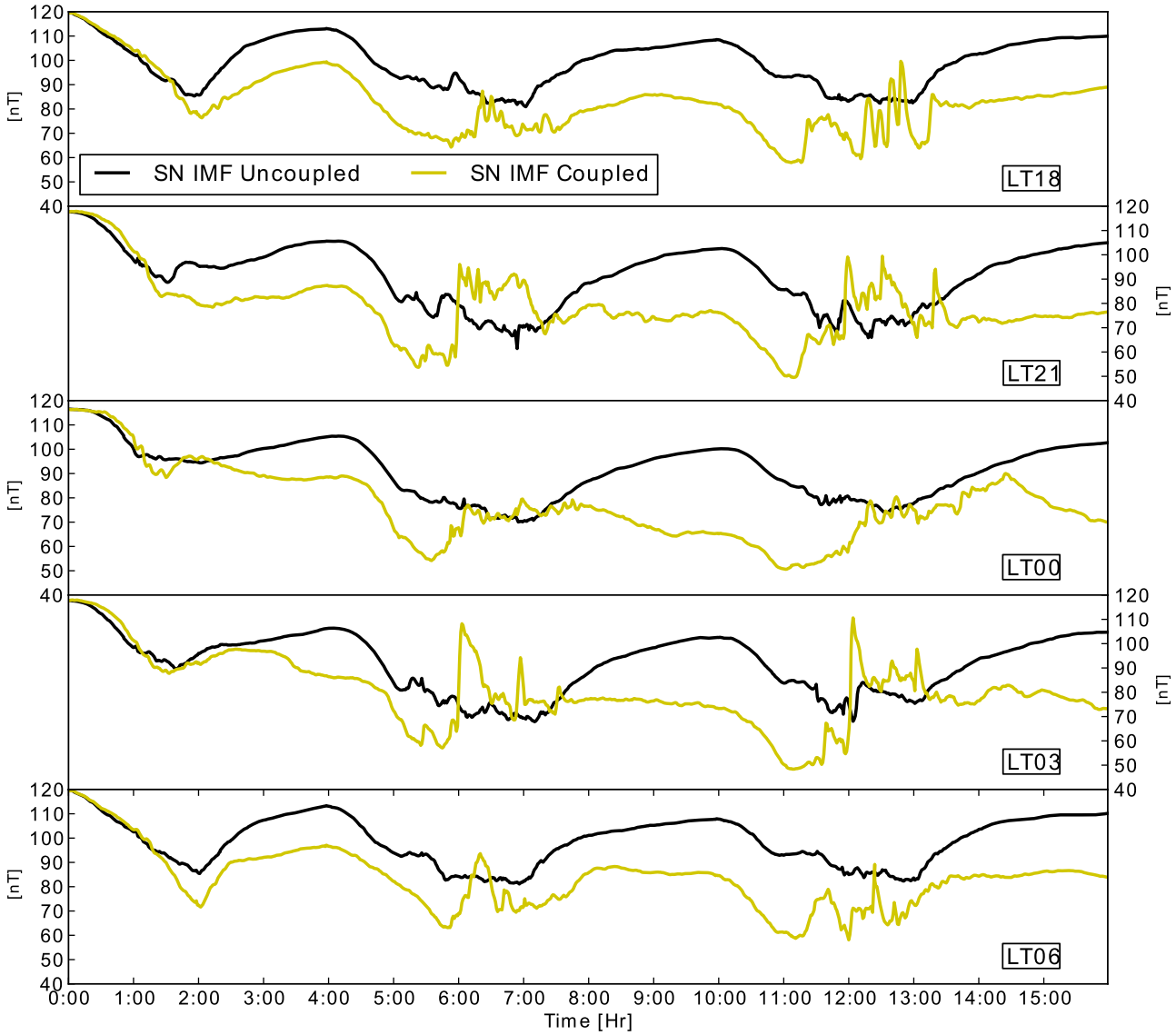

Figure 8. Same as Figure 7 but for SN IMF.

[52] Conservation of entropy in the LFM is shown in Figure 9a, which shows equatorial entropy and velocity vectors for the uncoupled S IMF run after 12 hours of continuous southward driving. The regions of low-entropy on the night side correlate strongly with earthward flow, so that the entropy gradient is perpendicular to the velocity. This suggests that entropy is conserved in the LFM, though deviations from strict conservation may be seen in Animation S1. These flow channel signatures originate near the open/closed boundary at -35 R_E in the tail. Two of the flow channels interact with the magnetosheath flow, producing Kelvin-Helmholtz waves near the dawn and dusk open/closed boundaries. Figure 9c shows mass content and contours of entropy, where adjacent contours differ by 40%. Along with Animation S1 for Figure 9, clearly the bulk of the mass content lies in the magnetosheath while the IMF is southward. At this time, the inner magnetosphere is empty for the uncoupled run, since there is no plasmasphere providing a source of mass.

[53] Next, we examine the effect of entropy flows on the ionosphere. Figure 9b shows Birkeland currents and contours of the electric potential for the uncoupled S IMF run, with the green curve designating the mapping of the open/closed boundary. Though they do not significantly modify the potential pattern, faint Birkeland currents can be seen equator-ward of the open/closed boundary on the night side. The equatorial flow channels seen in Figure 9a are visible as east-west entropy gradients in Figure 9d. The weak R-1 sense currents in the closed field region are clearly correlated with the longitudinal component of the entropy gradient, and by extension the entropy flow channels.

[54] Figure 10a shows field line entropy and velocity vectors in the equatorial plane for the coupled S IMF run and at the same time as Figure 9. The X-line is approximately 20 R_E tail-ward from that of the uncoupled run, making the closed field region of the coupled run significantly larger. The entropy parameter is higher than in the uncoupled case, with transient, earthward-flowing low-entropy bubbles

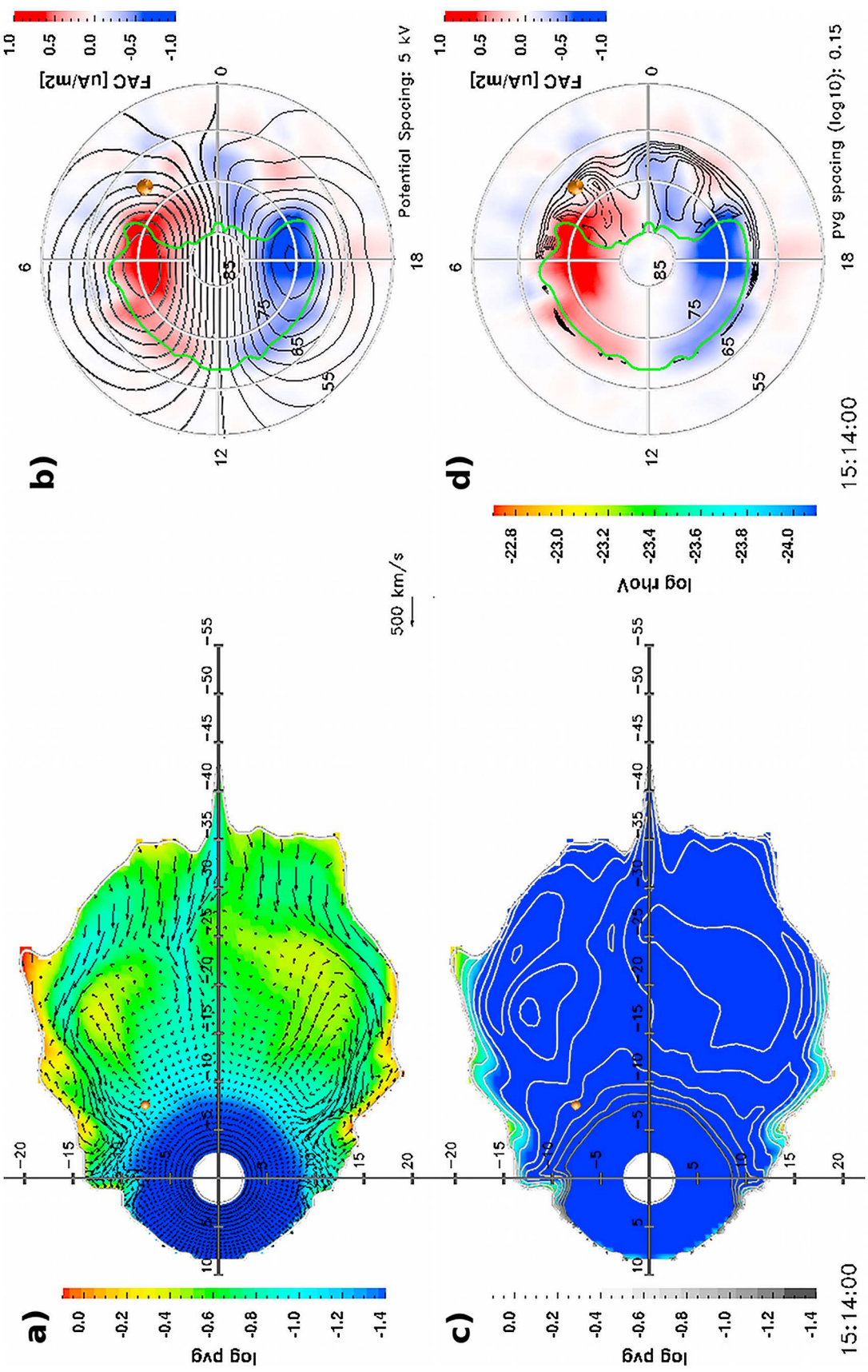

Figure 9. S IMF uncoupled run at 1514 UT. (a) Field line entropy (log pvg) and (c) mass content (log rhoV) are shown in the LFM equatorial plane, with the sun to the left. In Figure 9a, arrows indicate direction and strength of the fluid velocity, with a standard length shown at the bottom right. In Figure 9c, entropy contours are shown in grayscale with adjacent contours differing by 40%. (b) Birkeland current (color) and electric potential contours 5 kV apart. The green curve designates the open/closed boundary mapped onto the ionosphere. (d) Birkeland current and entropy contours, with the same spacing as those shown in Figure 9c.

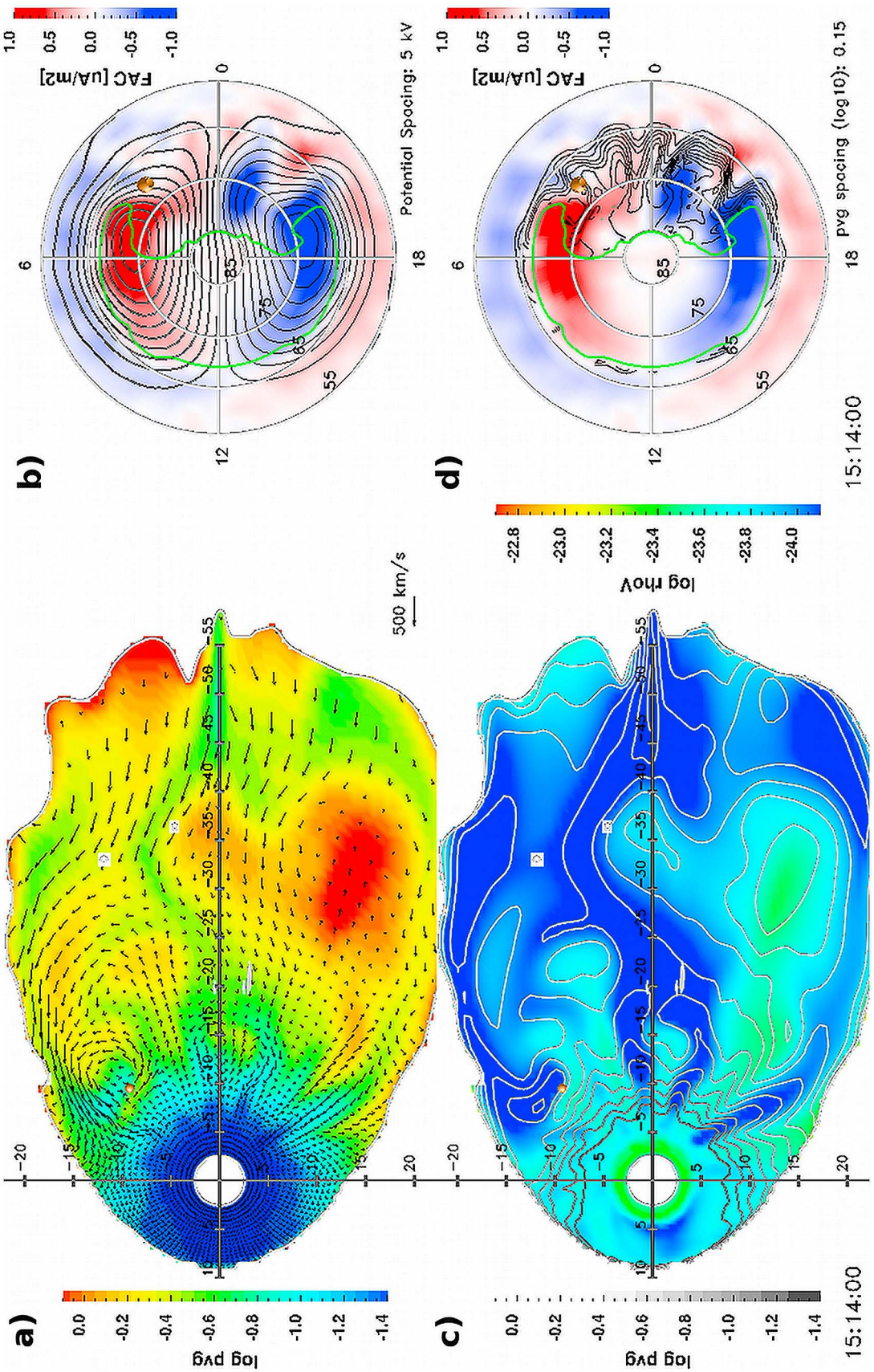

Figure 10. S IMF coupled run at 1514 UT. The same parameters as Figure 9 are plotted.

being more predominant. More flow vortices are produced, but separate from those created by shear flow near the flanks: one such vortex can be seen at the head of a low-entropy bubble at X = −5 R_E, Y = −10 R_E. Directly over this vortical structure, Figure 10c shows a region of high-mass/high-entropy content interacting with a low-mass/low-entropy flow. Such a configuration is typical of the coupled runs, and several more of these structures can be seen in Animation S2. Animation S2 also shows the diffusion of entropy and mass content following bubble injection into the RCM region.

[55] Figure 10d shows Birkeland current and contours of mapped entropy in the MIX domain for the coupled S IMF run. For reference, the orange glyph at the post-midnight sector in Figure 10d is the foot point mapping of the orange glyph in Figure 10c, at the edge of the (−5,−10) bubble. The equatorial plane shows a strong vortical structure appear near the location of the glyph. A corresponding Birkeland current signature appears at the ionospheric foot point several minutes later. Similarly, the contours of Figure 10d show strong east-west entropy gradients (mapped to low-entropy channels) alongside peaks in Birkeland current. This was observed to a lesser degree in the uncoupled run and is again consistent with the idea that some of the Birkeland current structures are associated with injections of low-entropy flux tubes.

[56] For both coupled and uncoupled S IMF runs, southward IMF intervals may be associated with transient low-entropy (bubble) injections, which trigger Birkeland current signatures in MIX. When the SN IMF runs are examined during the a northward IMF interval, no entropy flow structures are observed (see Animations S5 and S6 for coupled and uncoupled SN IMF runs). Instead, the entropy gradient relaxes to a smooth radial profile. Small rearrangements of entropy and density continue to occur, but at low velocities. From the ionospheric perspective, no low-latitude Birkeland current signatures were observed during this interval. In the uncoupled SN IMF run the picture is largely the same, except that the flux tube content is vanishingly small for the inner magnetosphere, due to the lack of a plasmasphere model.

[57] An examination of the fields is necessary to relate the entropy flows to the perturbations seen in the magnetic field at geosynchronous orbit. Figures 11a and 11b show LFM equatorial B_z with the dipole subtracted, together with entropy contours for the uncoupled and coupled S IMF runs, respectively. The magnetic field enhancement occurs within the entropy channel and is intensified near the head of the channel. These enhancements reach geosynchronous orbit in the coupled runs. The local times of Figure 7 are marked in Figure 11a. Comparing several of the field enhancements in Animation S3 for Figure 11a with the oscillations in Figure 7 shows that the two are strongly correlated. After reaching the ring current region, these enhancements slowly drift east or west depending on whether the bubble entered the post or pre-midnight sector. In the uncoupled code, the field enhancements are similar, but they do not reach geosynchronous orbit; instead, they immediately propagate toward the flanks and appear to interact strongly with the boundary layer.

[58] The presence of field enhancements near the head of the transient flow suggests that the low-entropy channels may be associated with field dipolarizations. The plasma-β may confirm that the flows are associated with localized dipolarization of the plasma sheet. Field line-averaged plasma-β for the S IMF uncoupled and coupled runs is shown in Figures 11c and 11d, respectively. The low-entropy channels, which are seen in the distortion of entropy contours, correspond with regions where plasma-$\beta \leq 1$. Where plasma-β is low and no flows are present, the gradient in plasma pressure would be in force-balance with field-line curvature. Therefore, the presence of earthward flows with low plasma-β suggests that the flows could be triggered by tail-ward dipolarizations that reduce field-line curvature, possibly as a result of reconnection.

4. Discussion

[59] Our initial results suggest that our coupling scheme for the MHD and ring current model is stable when the outer boundary of the ring current model actively limits the RCM to regions of low plasma-β. Using this modification, the occurrence of high-speed outflows in the LFM was prevented. In the following discussion, we highlight some of the effects that coupling has had on sub-domains of the magnetospheric system.

4.1. Ring Current

[60] The stand-alone MHD runs produced a low, diffuse pressure that peaks at the inner boundary of LFM (Figures 3a and 3c). However, observations show that pressure should peak and drop sharply earthward of 3 R_E [*Spence and Kivelson*, 1989]. The coupled runs produce a similar profile to observations, with peak occurring around 4 R_E (Figures 3b and 3d). Shielding of the low-latitude from the convection potential (see section 3.3) prevents plasma from reaching the inner boundary. Instead, gradient-curvature drift enforced by the RCM dominates the flow close to the Earth and causes the plasma to drift east- and westward rather than toward the inner boundary. Similarly, the depleted wedge seen in the uncoupled S IMF run is absent from the coupled run by the end of the simulation. This is also due to the gradient-curvature drift introduced by RCM, which moves plasma that would otherwise escape into the magnetosheath onto closed drift paths on the day side.

[61] The intensification of ring current pressure results in a reduction in the average magnetic field near Earth. This reduction continues indefinitely unless particle losses are enabled in the RCM. When losses are enabled, the field reduction approaches a minimum after 10–15 hours of southward IMF. This results from a balance of competing physical processes: particle loss due to charge exchange will reduce the energy content, while ring current injection causes intensification. Further studies are needed to investigate this balance and determine the extent to which low-entropy flows contribute to ring current pressure. The strength of the ring current pressure produces a measurable effect on the magnetopause location during northward IMF. The magnetopause in the coupled SN run is 1 R_E sunward compared to the uncoupled run. This supports results of *García and Hughes* [2007], who suggested that the lack of ring current pressure would explain why the LFM magnetopause was consistently earthward of empirical models by 0.5 to 1 R_E at noon.

4.2. Oscillations and Low-Entropy Flows

[62] Under steady driving with southward IMF, both uncoupled and coupled runs exhibit dynamic behavior

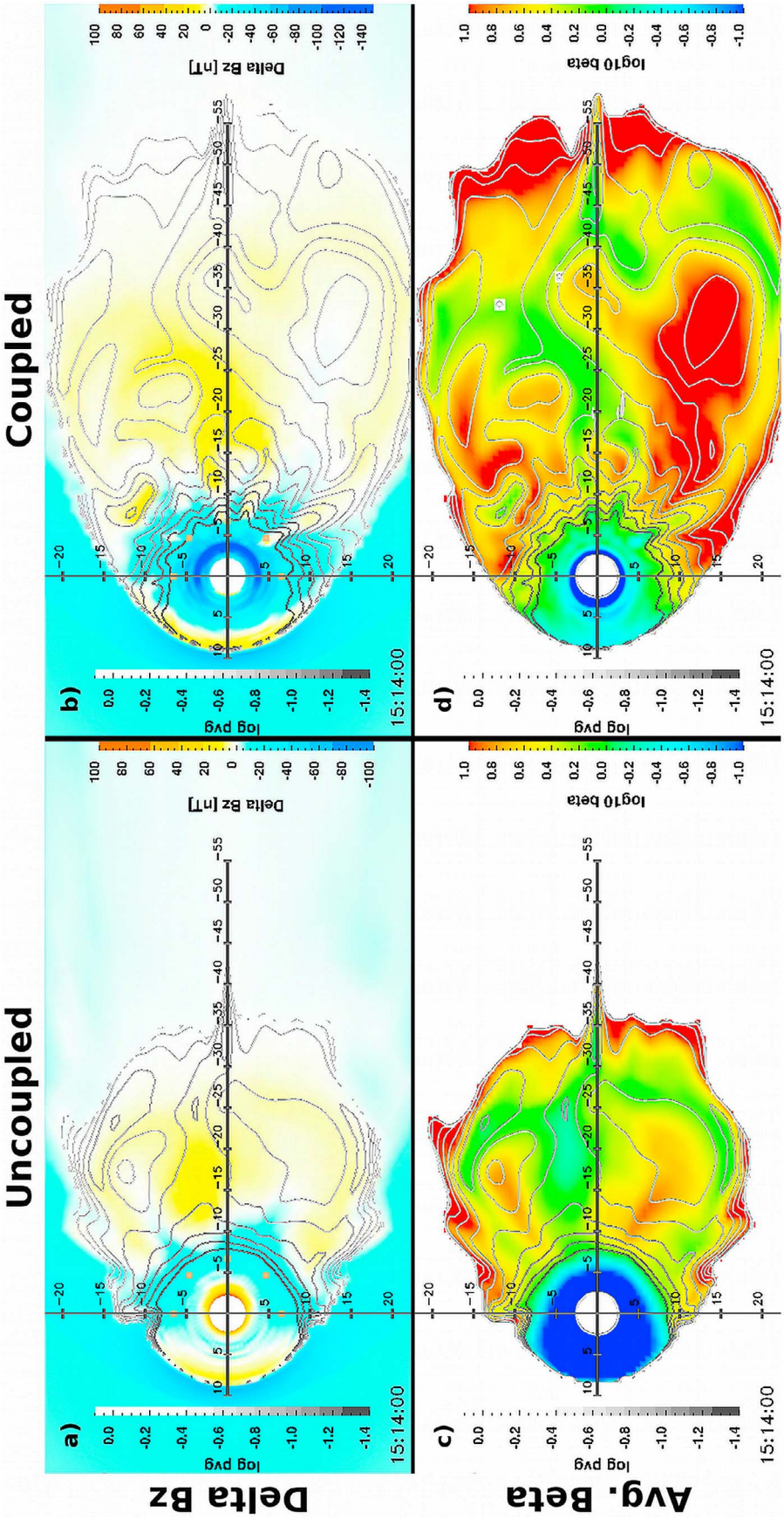

Figure 11. ΔB_z for (a) uncoupled and (b) coupled S IMF runs at 1514UT, together with the same entropy contours used in previous plots. Regions of field enhancement relative to the dipole are yellow and field depressions are in blue. The glyphs at geosynchronous orbit correspond to the local times of Figure 7. Field line plasma-β for (c) uncoupled and (d) coupled runs are shown on a log scale with entropy contours. -1 (dark blue) indicates a magnetic pressure $10\times$ that of the plasma pressure and $+1$ (red) the opposite.

through the creation and transport of low-entropy bubbles and high-entropy blobs (Figures 9 and 10). Figure 11 shows intensifications in the magnetic field at the head of low-entropy bubbles. If the bubbles reach geosynchronous orbit, they produce a perturbation in the magnetic field (Figure 7). This perturbation is characterized by an abrupt peak followed by gradual decline. Recent THEMIS observations show a similar profile for earthward-traveling dipolarization fronts [*Runov et al.*, 2009]. The observed dipolarization fronts are defined by a dip in B_z before the front, then a sharp increase, followed by a smooth decline. LFM-RCM-MIX produces field signatures with an abrupt peak followed by a slower decline and no prior dip, which is a slightly different profile from observed dipolarizations. The prior dip is typically on the ion inertial length scale [*Runov et al.*, 2009]. The code is not resolving such small-scale features due to a lack of resolution, and it may be missing physics in the ideal MHD formalism. For example, the Hall electric field, missing from ideal MHD, becomes important on ion inertial scales.

[63] The final inward propagation of dipolarization fronts in LFM-RCM-MIX may differ from those of observations. Statistically, these fronts are not typically observed inside of 10 R_E [*Ohtani et al.*, 2006]. *Dubyagin et al.* [2011] found from THEMIS observations that injection efficiency depends on the relative entropy of the low-entropy bubble and the background. Animation S2 for Figure 10 shows that the dipolarizations in the coupled code tend to reach geosynchronous orbit when the bubbles have entropy minimum at least a factor of 2 lower than the background. Further parameterizations of injections merit further study, such as bubble mass, speed, acceleration, and the dependence on grid resolution.

[64] The profile of magnetic perturbations we observe is also similar to the signatures found by *Taktakishvili et al.* [2007] when using BATS-R-US to drive the FokRC model with similar solar wind conditions to these S IMF runs (though with an IMF B_z of -15 nT). The oscillations seen in BATS-R-US were attributed to periodic reconnection events creating enhancements in the magnetic field that propagate inward from the tail. They observed oscillations with a period of 20 min or longer, while the period of oscillations in LFM is on the order of ten minutes. Though the timescales may be different, there is some circumstantial evidence that the oscillations observed in LFM may be similar in origin. The bubbles are produced during southward IMF just within the open/closed boundary, suggesting magnetic reconnection is a factor. However, the injection events occur more frequently in the coupled vs uncoupled runs though the same IMF conditions were used, suggesting that the ring current may be providing a feedback mechanism. One possibility is that the ring current pressure could be diffusing across field lines onto higher latitudes, which could supply higher pressures to the tail. Finally, the balance of day and night-side reconnection could also be involved in promoting low-entropy injections, since the X-line for the coupled run was tail-ward from that of the uncoupled run.

4.3. Plasmasphere

[65] The plasmasphere may give rise to several transient features that have a lasting effect on the model. Heavily loaded flux tubes extend from the edge of the plasmasphere into the plasma sheet. These create impediments to the entry of low-entropy bubbles. Whenever a low-entropy bubble pushes against a flux tube with high mass content, the bubble either squeezes past or gets diverted around the high-mass region. In either scenario, a strong vortical flow develops and a low-entropy wake persists for several minutes. In Animation S2 for Figure 10, the paths the bubbles take can be seen to depend on the history of previous injections. The channels created by injections appear to offer less resistance. Combined with high-mass flux tubes impeding the flow, the background entropy and density configuration is constantly restructuring. Northward intervals apparently restore the plasma sheet entropy and mass content to a smooth radial profile, thus permitting new bubbles to flow without interruption.

[66] The addition of the plasmasphere model also has consequences for plasma transport in the RCM modeling region. The added mass reduces the temperature of LFM near the outer boundary of RCM. The corresponding Maxwellian energy distribution that forms the RCM outer boundary condition is shifted toward lower energy. Particles in the lower energy channels of RCM have a reduced gradient-curvature drift, which allows them to drift closer to Earth. Numerical experiments with LFM-RCM-MIX without a plasmasphere resulted in only a weak ring current. Without the effect of plasmasphere cooling, the gradient-curvature drift term is too strong to permit a substantial ring current to develop. A cold component of the plasma in the MHD model may allow for ring current injection without the complexity introduced by the high mass content of the plasmasphere model. Future work coupling the RCM with the LFM multifluid code may resolve this issue [*Wiltberger et al.*, 2010; *Garcia et al.*, 2010].

4.4. Ionosphere

[67] Vortical flows can induce a twist in the magnetic field, creating Alfvén waves which propagate to the ionosphere as a pair of upward and downward Birkeland current signatures. Low-entropy bubbles produce vortical flows. Motion of Birkeland currents in the ionosphere is consistent with the motion of low-entropy bubbles. The ring current itself produces a much greater effect on the potential, producing shielding and overshielding as expected for the coupled run. Though the Region-2 current system is stronger in the coupled runs, the distribution of Birkeland currents is such that the polar cap potential drop is similar to that of the uncoupled run. A more detailed analysis of the geometry of the current patterns should clarify the role the Region-2 system has on the total polar cap potential.

5. Summary

[68] The aim of this paper has been to describe the coupled LFM-RCM-MIX code and report some preliminary results showing the influence of the coupling due to feedback from the RCM to the LFM. Several factors contributed both to the stability and response of the code to driving with moderate solar wind conditions. The two most prominent factors are the β switch and grid resolution. The β switch keeps the boundary of RCM consistent with the fundamental

assumption of quasi-static equilibrium and slow flow. However, the restricted boundary may be prohibiting the RCM from operating in regions where drift dynamics are still important. On the LFM side, some of the flows outside the coupling region may be due to interchange/ballooning instability, but it is possible they could be an artifact of grid resolution. Finite grid resolution would ultimately limit the amount of field line curvature that can be represented by the code as a response to increased ring current pressures imposed by RCM. Ruling out the effects of grid resolution is a work in progress. Apart from these caveats, we believe these results are representative of physical processes and not numerical instabilities. The LFM-RCM-MIX produced the following features that are not produced in the uncoupled runs:

[69] 1. The presence of RCM significantly improves shielding of the low latitude from the convection potential. This helps prevent low, diffuse pressure from reaching the inner boundary of LFM. The pressure peak near 4 R_E in the coupled results is consistent with observations. The build-up of pressure appears to reduce the magnetic field near Earth as approximated by D_{st}. If losses due to charge exchange or precipitation are neglected in the RCM, then the reduction in the field continues indefinitely as long as IMF B_z is southward. If losses are turned on, the D_{st} eventually levels off.

[70] 2. During southward IMF, the coupled run initially has a polar cap potential drop 20% higher than the uncoupled run, after which it approaches the uncoupled value over the course of several hours. This was accompanied by a 20-30% increase in the Region-1 current system. Region-2 currents were also higher in the coupled run by a factor of 2 and produce stronger shielding of the low-latitude region. However, the stronger region-2 system does not appear to affect the cross polar-cap potential significantly. A further investigation of their geometry will determine how the two current systems affect the total polar cap potential drop.

[71] 3. Oscillations in the magnetic field were observed at geosynchronous orbit and were strongest for the coupled runs near 2100 h and 0300 h LT. These oscillations are related to injections of low-entropy bubbles coming from the open/closed boundary in the tail. Since they only occur during southward IMF, we believe the bubbles are the result of magnetic reconnection in the magnetotail. Magnetic reconnection can deplete flux tubes of density and entropy, but further study is needed to verify if this is the cause. Once introduced into the stretched field region, the relatively lower entropy present in the bubbles causes them to migrate earthward, creating low-entropy channels that persist for several hours. The low-entropy injection path is highly dependent on the time history of injections, which occur approximately every 10 min in the coupled runs.

[72] 4. In the coupled run, the low-entropy injections are often diverted around high-mass flux tubes that appear to originate from the plasmasphere. This introduces a twist in the field that propagates into the ionosphere as an Afvén wave, resulting in a transient Birkeland current signature.

[73] The coupled LFM-RCM-MIX code provides a more complete picture of the magnetosphere, by playing off the strengths of the ring current and MHD formulations. Our coupling paradigm is most successful when the physical limitations of the constituent models are respected. The model produces several features that are not observed in the stand-alone MHD runs, and we are confident that continued efforts will bring the coupled model even closer to reality.

Appendix A: LFM Time-Averaging

[74] The running time averages for LFM pressure, density, and magnetic field are used to update the RCM. For an LFM variable q, the quantity $\langle q \rangle_{N+1}$ is the time average for the next time step in the simulation, and is given by

$$\langle q \rangle_{N+1} = \frac{\sum_{i=1}^{N} q_i dt_i + q_{N+1} dt_{N+1}}{T_N + dt_{N+1}} = \frac{\langle q \rangle_N (T_N - dt_{N+1})}{T_{N+1}} + \frac{q_{N+1} dt_{N+1}}{T_{N+1}}, \tag{A1}$$

where dt_i is the time step of LFM's solver at step i and is variable. T_N is the elapsed time from the start of the exchange up to step N. This formulation requires only the current time step q_{N+1} in order to update the average over the exchange.

Appendix B: LFM Decomposition

[75] At the RCM outer boundary, it is assumed that the plasma is Maxwellian as a function of energy, and that proton and electron densities are the same due to charge neutrality. It is further assumed the ion and electron temperatures are related by a constant factor $\alpha = 7.8$, based on observations by *Baumjohann et al.* [1989].

$$T_i = \frac{P}{k_B \rho (1 + 1/\alpha)} \tag{B1}$$

$$T_e = T_i / \alpha \tag{B2}$$

where k_B is the Boltzmann constant. For each charge species i, the energy distribution function $f_i(W_i)$ is given by

$$f_i(W_i) = \rho_i \left(\frac{m_i}{2\pi k_B T_i} \right)^{3/2} e^{-W_i / k_B T_i} \tag{B3}$$

where k_B is the Boltzmann constant. Using (11), in the energy-invariant λ-space this can be written

$$f_i(\lambda_{i,k}) = \rho \left(\frac{m_i}{2\pi k_B T_i} \right)^{3/2} e^{-\lambda_{i,k} V^{-2/3} / k_B T_i} \tag{B4}$$

Integrating over RCM energy channel limits ($\lambda_{\pm 1/2}$ defined by (17)) yields the RCM flux tube content $\eta_{i,k}$ for each channel centered at $\lambda_{i,k}$,

$$\eta_{i,k} = \rho V \left[\mathrm{Erf}(x_+) - \mathrm{Erf}(x_-) - \frac{2}{\sqrt{\pi}} \left(x_+ e^{-x_+^2} - x_- e^{-x_-^2} \right) \right], \tag{B5}$$

with

$$x_\pm = \sqrt{\frac{\lambda_{\pm 1/2}}{V^{2/3} k_B T_s}}, \tag{B6}$$

and

$$\mathrm{Erf}(x) = \frac{2}{\sqrt{\pi}} \int_0^x e^{-t^2} dt. \quad \text{(B7)}$$

Appendix C: Gallagher Plasmasphere Model

[76] Given the position $\mathbf{r}_{RCM}$ in the RCM ionospheric grid, the plasmasphere density $\rho_{gal}(\mathbf{r}_{RCM})[\mathrm{cm}^{-3}]$ is obtained from the radius of the equatorial mapping point $L(\mathbf{r}_{RCM})[\mathrm{R_E}]$ and the function

$$\log\left(\rho_{gal}(\mathbf{r}_{RCM})\right) = f(2.4 - L(\mathbf{r}_{RCM})/4) + (1-f)(4.5 - L(\mathbf{r}_{RCM})/2), \quad \text{(C1)}$$

where

$$f = \frac{1}{2}(1 + tanh(10(L(\mathbf{r}_{RCM}) - 4.5))). \quad \text{(C2)}$$

[77] Note that $L(\mathbf{r}_{RCM})$ is computed in the transfer of field-line averaged quantities from LFM. This functional form was determined from a fit to the Gallagher model [*Gallagher et al.*, 2000, Figure 1].

[78] **Acknowledgments.** This work has been supported by the Center for Integrated Space Weather Modeling under grant GC177024GA, NASA grant NNX08AM49G, and NASA GSRP Fellowship number NNX10AL82H. The National Center for Atmospheric Research is sponsored by the National Science Foundation. The authors are grateful to Richard Wolf for helpful discussions.

[79] Robert Lysak thanks the reviewers for their assistance in evaluating this paper.

References

Baumjohann, W., G. Paschmann, and C. A. Cattell (1989), Average plasma properties in the central plasma sheet, *J. Geophys. Res.*, *94*, 6597–6606, doi:10.1029/JA094iA06p06597.

Birn, J., M. Hesse, K. Schindler, and S. Zaharia (2009), Role of entropy in magnetotail dynamics, *J. Geophys. Res.*, *114*(A9), A00D03, doi:10.1029/2008JA014015.

Boyle, C., P. Reiff, and M. Hairston (1997), Empirical polar cap potentials, *J. Geophys. Res.*, *102*(A1), 111–125, doi:10.1029/96JA01742.

Brown, D., W. Henshaw, and D. Quinlan (1997), Overture: An object-oriented framework for solving partial differential equations, in *Scientific Computing in Object-Oriented Parallel Environments*, *Lect. Notes Comput. Sci.*, vol. 1343, edited by Y. Ishikawa et al., pp. 177–184, Springer, Berlin, doi:10.1007/3-540-63827.

Buzulukova, N., M. Fok, A. Pulkkinen, M. Kuznetsova, T. Moore, A. Glocer, and P. Brandt, G. Tóth, and L. Rastätter (2010), Dynamics of ring current and electric fields in the inner magnetosphere during disturbed periods: CRCM–BATS-R-US coupled model, *J. Geophys. Res.*, *115*, A05210, doi:10.1029/2009JA014621.

De Zeeuw, D., S. Sazykin, R. Wolf, T. Gombosi, A. Ridley, and G. Tóth, (2004), Coupling of a global MHD code and an inner magnetospheric model: Initial results, *J. Geophys. Res.*, *109*, A12219, doi:10.1029/2003JA010366.

Dubyagin, S., V. Sergeev, S. Apatenkov, V. Angelopoulos, A. Runov, R. Nakamura, W. Baumjohann, J. McFadden, and D. Larson (2011), Can flow bursts penetrate into the inner magnetosphere?, *Geophys. Res. Lett.*, *38*, L08102, doi:10.1029/2011GL047016.

Ebihara, Y., M. Fok, J. Blake, and J. Fennell (2008), Magnetic coupling of the ring current and the radiation belt, *J. Geophys. Res.*, *113*, A07221, doi:10.1029/2008JA013267.

Fedder, J., and J. Lyon (1987), The solar wind-magnetosphere-ionosphere current-voltage relationship, *Geophys. Res. Lett.*, *14*(8), 880–883, doi:10.1029/GL014i008p00880.

Fok, M., T. Moore, J. Kozyra, G. Ho, and D. Hamilton (1995), Three-dimensional ring current decay model, *J. Geophys. Res.*, *100*(A6), 9619–9632, doi:10.1029/94JA03029.

Fok, M., T. Moore, and R. Wolf (2001), Comprehensive computational model of Earth's ring current, *J. Geophys. Res.*, *106*(A5), 8417–8424, doi:10.1029/2000JA000235.

Gallagher, D., P. Craven, and R. Comfort (2000), Global core plasma model, *J. Geophys. Res.*, *105*, 18,819–18,833, doi:10.1029/1999JA000241.

García, K., and W. Hughes (2007), Finding the lyon-fedder-mobarry magnetopause: A statistical perspective, *J. Geophys. Res.*, *112*, A06229, doi:10.1029/2006JA012039.

Garcia, K. S., V. G. Merkin, and W. J. Hughes (2010), Effects of nightside O+ outflow on magnetospheric dynamics: Results of multifluid MHD modeling, *J. Geophys. Res.*, *115*, A00J09, doi:10.1029/2010JA015730.

Goodrich, C., A. Sussman, J. Lyon, M. Shay, and P. Cassak (2004), The CISM code coupling strategy, *J. Atmos. Sol. Terr. Phys.*, *66*(15–16), 1469–1479, doi:10.1016/j.jastp.2004.04.010.

Hain, K. (1987), The partial donor cell method, *J. Comput. Phys.*, *73*(1), 131–147, doi:10.1016/0021-9991(87)90110-0.

Harel, M., R. Wolf, P. Reiff, R. Spiro, W. Burke, F. Rich, and M. Smiddy (1981), Quantitative simulation of a magnetospheric substorm, 1. Model logic and overview, *J. Geophys. Res.*, *86*(A4), 2217–2241, doi:10.1029/JA086iA04p02217.

Heinemann, M., and R. Wolf (2001), Relationships of models of the inner magnetosphere to the Rice Convection Model, *J. Geophys. Res.*, *106*(A8), 15,545–15,554, doi:10.1029/2000JA000389.

Hu, B., F. Toffoletto, J. Raeder, R. Wolf, A. Vapirev, and D. Larson (2009), Two-way Coupled OpenGGCM and the Rice Convection Model, *Eos Trans. AGU*, *90*(52), Fall Meet. Suppl., Abstract SM51A-1317.

Hu, B., F. Toffoletto, R. Wolf, S. Sazykin, J. Raeder, D. Larson, and A. Vapirev (2010), One-way coupled OpenGGCM/RCM simulation of the 23 March 2007 substorm event, *J. Geophys. Res.*, *115*, A12205, doi:10.1029/2010JA015360.

Iijima, T., and T. Potemra (1978), Large-scale characteristics of field-aligned currents associated with substorms, *J. Geophys. Res.*, *83*(A2), 599–615, doi:10.1029/JA083iA02p00599.

Janhunen, P., K. E. J. Koskinen, and T. I. Pulkinen (1996), A new global ionosphere-magnetosphere coupling simulation utilizing locally varying time step, *Eur. Space Agency Spec. Publ.*, *389*, 205–210.

Jordanova, V., L. Kistler, J. Kozyra, G. Khazanov, and A. Nagy (1996), Collisional losses of ring current ions, *J. Geophys. Res.*, *101*(A1), 111–126, doi:10.1029/95JA02000.

Lee, J., and A. Sussman (2004), Efficient communication between parallel programs with InterComm, *Tech. Rep. CS-TR-4557 and UMIACS-TR-2004-04*, Univ. of Md. Inst. for Adv. Comput. Stud. and Dep. of Comput. Sci., College Park, Md.

Lemon, C., R. Wolf, T. Hill, S. Sazykin, R. Spiro, F. Toffoletto, J. Birn, and M. Hesse (2004), Magnetic storm ring current injection modeled with the Rice Convection Model and a self-consistent magnetic field, *Geophys. Res. Lett.*, *31*, L21801, doi:10.1029/2004GL020914.

Lyon, J., J. Fedder, and C. Mobarry (2004), The Lyon-Fedder-Mobarry (LFM) global MHD magnetospheric simulation code, *J. Atmos. Sol. Terr. Phys.*, *66*(15–16), 1333–1350, doi:10.1016/j.jastp.2004.03.020.

Merkin, V., and J. Lyon (2010), Effects of the low-latitude ionospheric boundary condition on the global magnetosphere, *J. Geophys. Res.*, *115*, A10202, doi:10.1029/2010JA015461.

Ogino, T., R. J. Walker, M. Ashour-Abdalla, and J. M. Dawson (1985), An MHD simulation of B_y-dependent magnetospheric convection and field-aligned currents during northward IMF, *J. Geophys. Res.*, *90*(A11), 10,835–10,842, doi:10.1029/JA090iA11p10835.

Ohtani, S., H. Singer, and T. Mukai (2006), Effects of the fast plasma sheet flow on the geosynchronous magnetic configuration: Geotail and GOES coordinated study, *J. Geophys. Res.*, *111*, A01204, doi:10.1029/2005JA011383.

Powell, K. (1994), An approximate Riemann solver for magnetohydrodynamics (that works in more than one dimension), *NASA Contractor Rep. 194902*, Inst. for Comput. Appl. in Sci. and Eng., NASA Langley Res. Cent., Hampton, Va.

Powell, K., P. Roe, R. Myong, T. Gombosi, and D. De Zeeuw (1995), An upwind scheme for magnetohydrodynamics, paper presented at 12th Computational Fluid Dynamics Conference, Am. Inst. of Aeronaut. and Astronaut., San Diego, Calif.

Powell, K. G., P. L. Roe, T. J. Linde, T. I. Gombosi, and D. L. De Zeeuw (1999), A solution-adaptive upwind scheme for ideal magnetohydrodynamics, *J. Comput. Phys.*, *154*(2), 284–309, doi:10.1006/jcph.1999.6299.

Pu, Z. Y., A. Korth, Z. X. Chen, R. H. W. Friedel, Q. G. Zong, X. M. Wang, M. H. Hong, S. Y. Fu, Z. X. Liu, and T. I. Pulkkinen (1997), MHD drift ballooning instability near the inner edge of the near-Earth plasma sheet and its application to substorm onset, *J. Geophys. Res.*, *102*(A7), 14,397–14,406, doi:10.1029/97JA00772.

Raeder, J., J. Berchem, and M. Ashour-Abdalla (1998), The Geospace Environment Modeling grand challenge: Results from a Global Geospace

Circulation Model, *J. Geophys. Res.*, *103*, 14,787–14,797, doi:10.1029/98JA00014.

Raeder, J., R. L. McPherron, L. A. Frank, S. Kokubun, G. Lu, T. Mukai, W. R. Paterson, J. B. Sigwarth, H. J. Singer, and J. A. Slavin (2001), Global simulation of the Geospace Environment Modeling substorm challenge event, *J. Geophys. Res.*, *106*(A1), 381–395, doi:10.1029/2000JA000605.

Ridley, A., T. Gombosi, and D. DeZeeuw (2004), Ionospheric control of the magnetosphere: Conductance, *Ann. Geophys.*, *22*, 567–584.

Runov, A., V. Angelopoulos, M. Sitnov, V. Sergeev, J. Bonnell, J. McFadden, D. Larson, K. Glassmeier, and U. Auster (2009), THEMIS observations of an earthward-propagating dipolarization front, *Geophys. Res. Lett.*, *36*, L14106, doi:10.1029/2009GL038980.

Song, Y., S. Sazykin, and R. Wolf (2008), On the relationship between kinetic and fluid formalisms for convection in the inner magnetosphere, *J. Geophys. Res.*, *113*, A08216, doi:10.1029/2007JA012971.

Spence, H., and M. Kivelson (1989), Magnetospheric plasma pressures in the midnight meridian: Observations from 2.5 to 35 R_E, *J. Geophys. Res.*, *94*, 5264–5272, doi:10.1029/JA094iA05p05264.

Stern, D. (1975), The motion of a proton in the equatorial magnetosphere, *J. Geophys. Res.*, *80*(4), 595–599, doi:10.1029/JA080i004p00595.

Taktakishvili, A., M. Kuznetsova, M. Hesse, and M. Fok, L. Rastätter, M. Maddox, A. Chulaki, T. Gombosi, and D. De Zeeuw (2007), Buildup of the ring current during periodic loading-unloading cycles in the magnetotail driven by steady southward interplanetary magnetic field, *J. Geophys. Res.*, *112*, A09203, doi:10.1029/2007JA012317.

Toffoletto, F., S. Sazykin, R. Spiro, and R. Wolf (2003), Inner magnetospheric modeling with the rice convection model, *Space Sci. Rev.*, *107*, 175–196, doi:10.1023/A:1025532008047.

Toffoletto, F., S. Sazykin, R. Spiro, R. Wolf, and J. Lyon (2004), RCM meets LFM: Initial results of one-way coupling, *J. Atmos. Sol. Terr. Phys.*, *66*(15–16), 1361–1370, doi:10.1016/j.jastp.2004.03.022.

Vasyliunas, V. (1970), Mathematical models of magnetospheric convection and its coupling to the ionosphere, in *Particles and Fields in the Magnetosphere*, pp. 60–71, D. Reidel, Dordrecht, Netherlands.

Volland, H. (1973), A semiempirical model of large-scale magnetospheric electric fields, *J. Geophys. Res.*, *78*(1), 171–180, doi:10.1029/JA078i001p00171.

Wiltberger, M., W. Wang, A. Burns, S. Solomon, J. Lyon, and C. Goodrich, (2004), Initial results from the coupled magnetosphere ionosphere thermosphere model: Magnetospheric and ionospheric responses, *J. Atmos. Sol. Terr. Phys.*, *66*(15–16), 1411–1423, doi:10.1016/j.jastp.2004.03.026.

Wiltberger, M., S. Elkington, T. Guild, D. Baker, and J. Lyon (2005), Comparison of MHD simulations of isolated and storm time substorms, in *The Inner Magnetosphere: Physics and Modeling*, *Geophys. Monogr. Ser*, vol. 155, edited by T. I. Pulkkinen, N. A. Tsyganenko, and R. H. W. Friedel, pp. 271–281, AGU, Washington, D. C., doi:10.1029/155GM29.

Wiltberger, M., W. Lotko, J. G. Lyon, P. Damiano, and V. Merkin (2010), Influence of cusp O^+ outflow on magnetotail dynamics in a multifluid MHD model of the magnetosphere, *J. Geophys. Res.*, *115*, A00J05, doi:10.1029/2010JA015579.

Wolf, R. (1983), The quasi-static (slow-flow) region of the magnetosphere, in *Solar-Terrestrial Physics: Principles and Theoretical Foundations*, vol. 104, edited by R. L. Carovillano and J. M. Forbes, pp. 303–368, D. Reidel, Dordrecht, Netherlands.

Wolf, R., and R. Spiro (1983), The role of the auroral ionosphere in magnetospheric substorms, in *High-Latitude Space Plasma Physics*, edited by B. Hultqvist and T. Hagfors, pp. 19–38, Plenum, New York.

Wolf, R. A., Y. Wan, X. Xing, J.-C. Zhang, and S. Sazykin (2009), Entropy and plasma sheet transport, *J. Geophys. Res.*, *114*, A00D05, doi:10.1029/2009JA014044.

Wolf, R. A., C. X. Chen, and F. R. Toffoletto (2012a), Thin-filament simulations for Earth's plasma sheet: Interchange oscillations, *J. Geophys. Res.*, doi:10.1029/2011JA016971, in press.

Wolf, R. A., C. X. Chen, and F. R. Toffoletto (2012b), Thin filament simulations for Earth's plasma sheet: Tests of validity of the quasi-static convection approximation, *J. Geophys. Res.*, doi:10.1029/2011JA016972, in press.

Yee, K. (1966), Numerical solution of initial boundary value problems involving maxwell's equations in isotropic media, *IEEE Trans. Antennas Propag.*, *14*(3), 302–307, doi:10.1109/TAP.1966.1138693.

Zaharia, S., V. K. Jordanova, M. F. Thomsen, and G. D. Reeves (2006), Self-consistent modeling of magnetic fields and plasmas in the inner magnetosphere: Application to a geomagnetic storm, *J. Geophys. Res.*, *111*, A11S14, doi:10.1029/2006JA011619.

Zaharia, S., V. K. Jordanova, D. Welling, and G. Tóth (2010), Self-consistent inner magnetosphere simulation driven by a global MHD model, *J. Geophys. Res.*, *115*, A12228, doi:10.1029/2010JA015915.

Zhang, J.-C., R. A. Wolf, S. Sazykin, and F. R. Toffoletto (2008), Injection of a bubble into the inner magnetosphere, *Geophys. Res. Lett.*, *35*, L02110, doi:10.1029/2007GL032048.

J. Lyon, Department of Physics and Astronomy, Dartmouth College, Hanover, NH 03755, USA.

V. Merkin, Johns Hopkins University Applied Physics Laboratory, Johns Hopkins University, 11100 Johns Hopkins Rd., Laurel, MD 20723, USA.

A. Pembroke, S. Sazykin, and F. Toffoletto, Department of Physics and Astronomy, Rice University, 6100 Main St., Houston, TX 77005, USA. (asher.d.pembroke@rice.edu)

P. Schmitt and M. Wiltberger, High Altitude Observatory, National Center for Atmospheric Research, 3090 Center Green Dr., Boulder, CO 80301, USA.